SYNTHESIS OF LUMINESCENT $SrAl_2O_4:Eu^{2+},Dy^{3+}$ NANOMATERIALS FOR EMERGENCY DISPLAYS

VICTOR SAIDI KADENGE

A THESIS SUBMITTED IN PARTIAL FULFILLMENT OF THE REQUIREMENTS FOR THE AWARD OF THE DEGREE OF MASTER OF SCIENCE IN PHYSICS OF THE

UNIVERSITY OF EMBU

AUGUST, 2024

DECLARATION

This thesis is my original work and has not been presented for a degree in any other university.

Signature…… Date **……**

Victor Saidi Kadenge

B525A/1359/2020

Department of Physical Sciences

This research project has been submitted for examination with our approval as the University Supervisors

Signature…… Date…….

Dr. Ali Halake Wako

Department of Physical Sciences

University of Embu.

Signature…… Date…….

Dr. MillienKawira

Department of Physical Sciences

University of Embu.

Signature…… Date…….

Dr. Sharon Kiprotich

Department of Physical and Biological Sciences

Murang'a University of Technology.

DEDICATION

This thesis is dedicated to Almighty God for His love and mercy towards me and my family

ACKNOWLEDGMENT

I would like to convey my appreciation to God for bestowing upon me the chance to complete this research. I attribute my scholastic success to divine intervention and give credit to God. The guidance and support provided by my supervisors, Dr. Ali, Dr. Sharon, and Dr. Kawira, have been indispensable in my pursuit of completing my master's degree. I am immensely grateful to them for their invaluable support in enabling me to achieve academic and personal milestones by consistently challenging and motivating me. This research would not be feasible without their efforts. I am grateful to Dr. George S. Nyamato, Dr. Joan Oguna, and Mr. Mukono, who are all members of the faculty, for their assistance and support. I express my gratitude to the Murang'a University of Technology Analytical Laboratory and the Meneng'ai Geothermal power plant for granting me access to their facilities for doing my research, offering me indispensable support, and furnishing me with invaluable advice. The unwavering aid, backing, scholarly discourse, and camaraderie provided by my fellow graduate students, specifically Peter Anuda, Samuel Waithera, David Kitheka , and Francis Kuria, greatly enriched my experience at the University. Finally, I would want to convey my appreciation to my mother, my wife Victoria Chea and my son, Myles Fadhili, for their constant encouragement and moral support during this journey.

TABLE OF CONTENTS

LIST OF TABLES

LIST OF FIGURES

LIST OF ABBREVIATIONS AND ACRONYMS

CB	Conduction Band
CRT	Cathode ray tube
FEDs	Field emission displays
FTIR	Fourier Transform Infrared
FWHM	Full Width at Half Maximum
JCPDS	Joint Committee on Powder Diffraction Standards.
LCDs	Liquid crystal displays
LEDs	Light emitting diodes
LLPs	Long lasting phosphors
NPs	Nanosized phosphors
PDPs	Plasma display panels
Persl	Persistent luminescence
PL	Persistence luminescence
SAED	$SrAl_2O_4:Eu^{2+},Dy^{3+}$
UV	Ultraviolet
UV-Vis	Ultra Violet Spectroscopy
VB	Valence Band
VFDs	Vacuum fluorescent displays
XRD	X-Ray diffraction

ABSTRACT

$SrAl_2O_4:Eu^{2+},Dy^{3+}$ are phosphors with unique tuneable properties. This work comprises of several aspects of strontium-aluminate phosphor doped with rare earth metal ions ($SrAl_2O_4:Eu^{2+},Dy^{3+}$). In particular the optical and structural properties of the long afterglow $SrAl_2O_4:Eu^{2+},Dy^{3+}$ phosphors prepared by urea-nitrate solution-combustion method were investigated. The solution-combustion method is more efficient because phosphors with high efficiency were obtained at low temperature in a very short period of time (5 min). The effects of varying concentration of host matrix composition (Sr:Al), co-dopant and growth temperature on the structural and optical properties of the $SrAl_2O_4:Eu^{2+},Dy^{3+}$ phosphors were studied. Temperature is a critical variable in thermodynamics that has a substantial impact on the shape, size, and surface properties of the produced nanoparticles. A study was carried out to investigate the influence of this factor on the optical and structural characteristics of $SrAl_2O_4:Eu^{2+}$, Dy^{3+}. The results of the X-ray diffraction (XRD) analysis reveal that the 2mol % favored the formation of monoclinic phase. The X-ray diffraction patterns for all the $SrAl_2O_4:Eu^{2+},Dy^{3+}$ NPs exhibited a highly crystalline and monoclinic structure of $SrAl_2O_4:Eu^{2+},Dy^{3+}$ with no impurity phases. The values of the crystallite sizes range from 35 to 42 nm and 32.23 to 29.7 nm for the NPs prepared at different furnace temperatures and varied concentrations respectively. A similar trend was observed also for other growth on varying concentration of host matrix composition (Sr:Al). The research on the impact of Dy^{3+} concentration revealed that the average lattice constants 'a' were determined to be a = 0.84470 nm, indicating a decreasing tendency with higher degrees of Dy^{3+} doping and Al/Sr ratios. The results closely match the bulk $SrAl_2O_4:Eu^{2+}$, Dy^{3+} lattice constants provided in the standard JCPDS data file No.34-0379. The ultraviolet and visible analysis (UV-Vis) displayed well-resolved absorption maxima which were red shifted upon increase in growth temperature and varying concentration of host matrix composition (Sr:Al) concentration. There was an inverse relation between the bandgap and the reaction parameters under study (reaction time, growth temperature and varying concentration of host matrix composition (Sr:Al). The band gap energies of the $SrAl_2O_4:Eu^{2+}$, Dy^{3+} nanoparticles were adjusted within the range of approximately 5.62 to 5.4 eV by increasing the temperature of the furnace. The band gaps of $SrAl_2O_4:Eu^{2+}$, Dy^{3+} exhibited a range of 6.5 to 5.5 eV as the concentration of Dy^{3+} during growth increased. The sample of $SrAl_2O_4:Eu^{2+}$, Dy^{3+} NPs, synthesized with a doping of 0.4 mol% Dy^{3+}, grown in a growth medium with a ratio of 2 Al/Sr, and prepared at 700 ºC, exhibited optimal crystallinity, minimal lattice stress, and favorable optical characteristics.

CHAPTER ONE

INTRODUCTION

1.1. General Introduction

As for the US Ministry of Energy, lighting constitutes 14% of the overall energy consumption in the US and 21% of the power usage in buildings [1]. There is an increasing interest in creating more efficient lighting systems which may decrease energy usage and the emission of pollutants from fossil fuel power plants, while yet delivering effective lighting for different purposes. Scientists researching luminous materials have long sought to develop effective phosphors for lighting purposes. The term "phosphor" refers to a type of solid substance that can transform absorbed energy into light that is observable, without becoming incandescent. Humans have enormous lighting requirements to defend themselves better at night [2]. Additionally, they require light to increase their work hours and for nighttime entertainment [3]. Since the dawn of human history, people have continuously created new lighting systems to satisfy this requirement. Lighting has advanced dramatically from fires made of wood to torches, oil flames, fluorescent tubes, LEDs, and persistence luminescence (PL) from nanocrystalline powders [4]. These advances in lighting technology have significantly impacted the typical way of living.

Like the urge to connect with other people, technological advances underwent tremendous development as a result [5]. From rock cliff faces to telecommunication methods, technology has advanced to greater heights. The emergence of electronic gadgets has dramatically accelerated the distribution of information [6].Since the data kept within technology is unseen by normal sight, there arose a demand for the representation of neglected details. As a result, display devices like FEDs and PDPs have been created to act as an interface between people and electronics. A sizable fraction of luminous nanomaterials are utilized in display devices to transform this eye-catching information [7].

An already overburdened global energy grid is under pressure from rising demand for such smart device. Therefore, it is crucial to produce cost-effective, green glowing substances that have great colours rendering capabilities, high colour strength, high

luminous performance, extended retention, and a small budget. Long afterglow is one of the most popular luminescent materials which glows for a hours even when source of light is withdrawn [8, 9]. The recombination of stored electrons and thermally released holes can account for this long-lasting brilliant radiation [10]. Oxide-based inorganic nanomaterials doped with divalent europium have excellent physical and thermal endurance, variable wavelengths of emission spanning UV to red, and minimal toxic exposure, making them highly valuable [11]. These phosphors are essential in various scholarly and industrial operations such as the creation of cathode ray tubes, laptops and smartphones. The lowest $4f^6 5d^1$ excited state's parity-permitted electronic transition into the $4f^7$ ground state is what gives Eu^{2+} based phosphors their characteristically broad emission bands upon excitation [12]. The host lattice significantly impacts the emission wavelength and is connected to how this state is positioned about the $4f^7$ ground state [13].

The key influencing factors inside the host structure are the quantity of cationic locations that Eu^{2+} will coordinate with, the expansion influence brought of ligands on the electron orbital, and the length of the connection between the cation and its ligands [14]. Photoluminescence from nanomaterials like $SrAl_2O_4:Eu^{2+}$, Dy^{3+} had been determined by Matsuzawa *et al*, in 1996 [15] which has become the focus of ongoing study. The spectral characteristics of nanoparticles remain unchanged compared to their larger counterparts. This is true even when the particles are reduced to a nanoscale, which improves the practicality of luminescent materials due to increased density, reduced light scattering, and easy dispersal in fluids [16]. Afterglow nanoparticles have been used in many different applications, like writing and printing inks, plasma display phosphors, traffic signs, safety indicators on emergency systems, and bioimaging [1]. Afterglow materials solve the auto fluorescence issue in bioimaging when fluorescent components already present in living cells are activated [17].The best results can be obtained if the excitation light is obstructed before the indicator begins glowing. The afterglow light is used to generate oxygen in singlet form, which kills cancer cells in PDT (photodynamic therapy) light sources. This is another biological application. Numerous authors, such as Yang *et al.* 2012 [18] have extensively debated theories to explain the afterglow mechanism.

Typically, the development of an electron and hole trapping system is linked to the persistence luminescence in strontium aluminate structure activated with Eu^{2+} and Dy^{3+}. According to one of the ideas, the afterglow effect happens when an excited hole from $Eu^{2+}$is thermally triggered released to the VB and then entrapped by Dy^{3+} [19]. The extra thermally accelerated liberation of the electron hole from Dy^{4+} and coupling with Eu^{2+} results in afterglow illumination [20]. Along with the mechanism underlying the persistence photoluminescence influence on alkali aluminate activated with rare earth metals another aspect of the $SrAl_2O_4:Eu^{2+},Dy^{3+}$spectroscopic behavior is still being heavily debated. The $4f^65d^1$ to $4f^7$ electronic shift of europium ion is known in the literature as the main cause of the Gaussian-shaped band that is prominent in the emission spectra of $SrAl_2O_4:Eu^{2+},Dy^{3+}$ at room temperature [20].

In contrast, dividing the emission spectra into two bands results from cooling down Eu^{2+} doped $SrAl_2O_4$to extremely low temperatures. Several authors have successfully used combustion synthesis to prepare $SrAl_2O_4:Eu^{2+},Dy^{3+}$nanoparticles[21].Finely crystallized chemicals, especially heavy oxides include aluminates, orthosilicates, and chromites, are prepared using combustion synthesis. It entails an exothermic redox process that occurs involving an organic fuel such as urea and an oxidant like metal nitrates[22]. According to reports, urea also serves as a dispersant for the nanoparticles. The current study used combustion synthesis to create $SrAl_2O_4:Eu^{2+}$, Dy^{3+} NPs for informational signage, analysis and explanation of their outstanding optical and structural features.

1.2. Preferential pedestrian pathway

Substantial pedestrian usage is easily accessible on preferred routes. The ability to pinpoint the position of luminescent signages which includes an evacuation strategy, is excellent along these pathways (such as corridors, stairwells, and safety exits). The proper placement of luminescent items and materials along escape routes makes it possible to obtain details concerning safety signaling during a quick evacuating operation. The preferred pedestrian route maintains a black background in the dark to create an eye-catching contrast with luminescent materials used for safety signaling.

Figure 1.1: Preferential pedestrian pathway with a photoluminescent signaling [23]

1.3. Statement of the Problem

Occupational safety and health has been a significant concern for many organizations. During emergencies such as terrorist attacks, fire outbreaks, earthquakes, or any other form of insecurity, the first emergency step is switching off electricity and evacuating people. Leaving the building or evacuating people at this point becomes difficult due to dark exits, pathways and corridors since many workplaces rely on electricity to light up these areas. In contrast, those in rural areas don't have electricity at all. Many accidents in workplaces, residential areas, roads and hospitals have been reported to cause grievous injuries and even deaths. These accidents can be attributed to poorly lit passages, corridors and stairs, lack of emergency exit signs, frequent electricity blackouts or total lack of electricity, especially in rural areas.

Currently, many workplaces in Kenya use exit and warning signs which rely solely on electricity. In contrast, others are just reflectors that are not visible at night and when there is no electricity. These pose a significant danger during sudden power outages, making it difficult to exit buildings and workplace areas. The cost of electricity bills also compounds the problem even more, making people resort to other lighting forms such as firewood, candles, and kerosene lamps. These forms of lighting produce smoke containing carbon monoxide, which negatively impacts the

environment and people's health. This research intends to solve the problem by ensuring that all hazardous areas, safe areas, assembly points, ambulances, emergency exits, and locations of fire extinguishers and alarms are clearly marked and visible even in the dark using efficient signage fabricated using low cost locally available materials which are not harmful to the environment and human health

1.4. Research Questions

1. What is the impact of temperature on the optical properties of $SrAl_2O_4:Eu^{2+},Dy^{3+}$ phosphor?
2. Does the ratio of europium nitrate to dysprosium nitrate affect the luminescence properties of$SrAl_2O_4:Eu^{2+},Dy^{3+}$ phosphor?
3. What is the effect of the stoichiometry (Sr: Al) on the structural and luminescent properties?

1.5. Objectives

1.5.1. General Objective

To establish the effectiveness of synthesized $SrAl_2O_4:Eu^{2+},Dy^{3+}$, phosphor as emergency warning signs and indicators for occupational safety and health.

1.5.2. Specific Objectives

1. To synthesize the Strontium aluminate $SrAl_2O_4:Eu^{2+},Dy^{3+}$ phosphor.
2. To determine the effect of growth temperature of $SrAl_2O_4:Eu^{2+},Dy^{3+}$ phosphor on the optical and structural properties.
3. To determine the effect of co-dopant concentration of $SrAl_2O_4:Eu^{2+},Dy^{3+}$ phosphor on the optical and structural properties.
4. To determine the impact of host material composition of $SrAl_2O_4:Eu^{2+},Dy^{3+}$ phosphor on the optical and structural properties

1.6. Justification of the Study

Luminescent or glow-in-the-dark nanomaterials are suitable for marking building exit routes and acting as a lighting source during electricity failure. This innovative alternative uses Strontium aluminate phosphor, $SrAl_2O_4:Eu^{2+},Dy^{3+}$ which gives off deep greenish-yellow light for long hours compared to other phosphor. International standards recommend the green emission color for safety signs. This has been guided by the physiology of the human eye adaptation to vision in the dark since the human eye can detect minimal light changes. These $SrAl_2O_4:Eu^{2+},Dy^{3+}$ material absorbs

radiation energy from the sun and other light sources, store it, and then emits it as light in the dark. It is suitable for security and emergency lighting. It can also be used in rural areas without electricity and for other outdoor uses such as billboards, safety jackets and sportswear. These phosphors are more suitable for emergency applications as compared to all other sources of light since they are cheap and easy to fabricate, they require no maintenance and technical servicing after installation, they have no running cost or bills, they are more durable and renewable source of energy which can withstand adverse weather conditions and they emit clean evenly distributed light which is environmentally safe since they don't produce any contaminants to pollute the environment and also they don't contain any kind of radioactive elements.

Table 1.1: Colour indicators for warning signs [24]

Colour	Meaning	Instruction and information
Red	Advisory notice	Unpredictable conduct
	Hazard signal	Stop, shutdown, emergency cut out devices
	Apparatus for fighting fires	Location and identification
Yellow	Alert symbol	Be watchful, take precautions and look over
Blue	Obligatory sign	Particular conduct
Green	Escape route	Door exit
	Sign for first aid	
	Zero threat	Back to normal

CHAPTER[o1] TWO

LITERATURE REVIEW

2.1 Persistent Luminescent Phosphors

Persistent luminescence (PersL) is a unique optical property in which, after absorbing photons, the excitation state gradually returns to the ground's state for periods significantly longer than anticipated. Persistent luminescence, often referred to as phosphorescence, afterglow, or afterglow phosphorescence, is a scientific phenomena that can endure for varying durations, ranging from a few seconds to several hours or even days [25]. A luminous core, typically a transitional metal, is found in crystalline inorganic semiconducting or insulating materials, referred to as a host lattice. Electronic transitions in the luminous core are visible in the electromagnetic spectrum's visible range [26]. The resulting interaction between the host crystal structure and the luminescence center give rise to PersL and make up this class of persistent luminescent phosphors (PLPs). The discovery of PersL dates back at least one thousand years to the ancient Chinese. They mixed colors with a particular type of pearl shell or use in artwork and noticed visible light emitting from their paintings [10]. The Bologna stone, also known as the Bologian Phosphor, found by Vincenzo Casariolo, is the first scientific example of a PLP reported in 1602 [27]. The naturally occurring afterglow observed was later attributed to impurities identified as BaS [14]. However, the intentional incorporation of impurities, also known as "killers," to induce long emission lifetimes was first introduced by substituting CaS with bismuth in 1866 [16]. Long luminescent lifetimes were significantly advanced by the discovery of Cu^{+} and Co^{2+} substituted ZnS in the early 20th century [28]. The long luminescent lifetime produced in ZnS:Cu^{+},Co^{2+} enabled the material to become commercially available in products such as luminous paints and watch dials ushering in an area of investigating new applications. Additional use in emergency signage and novelty items like children's toys has since been created with the discovery of the transformative PLP, green-emitting $SrAl_2O_4$:Eu^{2+}, Dy^{3+}, which was first reported in 1996 [29]. There are now several commercially available PLPs with various emission colors. In recent years, the use of PLPs has extended into bioanalytical applications that have been of great importance in advancing medical devices and imaging [30]. Table 2.1 shows the PersL nanomaterial and their afterglow lifespan.

Table 2.1: Overview of Significant Persistent Luminescent Phosphors Studied Over the Last Century [31]

Host material	Luminescent centre	Co-dopant	Lifetime
ZnS	Cu	Co^{2+}	3hrs
CaS	Bi	----	20min
$CaGa_2S_4$	Eu	----	30min
$Y_2O_2S_2$	Eu	Mg^{2+}	3hr
$Ca_2Si_5N_8$	Eu	Tm^{3+}	1hr
$SrAl_2O_4$	Eu	Dy^{3+}	30hr
$CaAl_2O_4$	Eu	Nd^{3+}	5hr
$Sr_4Al_{25}O_{14}$	Eu	Dy^{3+}	20hr
$Sr_2MgSi_2O_7$	Eu	Dy^{3+}	10hr
$ZnGa_2O_4$	Cr	----	1hr
$MgGa_2O_4$	Cr	----	15min

2.2 Luminescence

The phenomenon of illumination is the process through which substances like phosphors give off light [32]. The excitement of such substance leads to this effect when atoms in states of more tremendous energy unite with holes in states with lower state. Stokes' law states that the luminescence intensity must be less than the excitation wavelength for the reaction to occur [6].

2.3 Classification of luminescence

When a substance emits light beyond the time it takes for the eye to detect it, we say that it "luminesces." Luminescence is a release of light beyond that attributed to the black body's energy. Afterglow, light is produced from any power—chemical energy included—introduced into the mechanism [19]. Thus, luminescence has been sorted into various categories based on the nodes of excitations. Several different luminescence phenomena have been seen in either natural or artificial materials. Their names always have some connection to the stimulating agent that is responsible for the luminosity.

2.3.1 Bioluminescence

Bioluminescence refers to a phenomenon when living creatures emit light [33]. This constitutes a subtype of chemiluminescence where some chemical reaction takes place. An amino acid known luciferase and a afterglow substance termed luciferin are responsible for the primary chemical process in bioluminescence [34]. The reaction entails the process of oxidizing luciferin, facilitated by the enzyme luciferase to enhance the reaction rate. Bioluminescence occurs mainly in marine vertebrates and invertebrates, some fungi, bioluminescent bacteria and terrestrial invertebrates such as fireflies [9].

Figure 2.1: Firefly and female glowworm showing bioluminescence [34]

2.3.2 Chemiluminescence

Chemiluminescence also known as Chemoluminescence is the emission of light due to any chemical reaction [35]. Here, some emission of heat can also take place. In this type of luminescence, electronic transitions occur and emits light when it relaxes from its excited states to the ground state. Elemental white phosphorous glow green in moist air is the best example of chemiluminescence. Luminol is a well-known chemiluminescent substance that finds blood traces during criminalistic problems [36]. Fe^{2+} ion present in blood Hb acts as a catalyzer and brings luminol to its light-emitting configuration. Oxidation of luminol with hydrogen peroxide gives blue or bluish-green chemiluminescence.

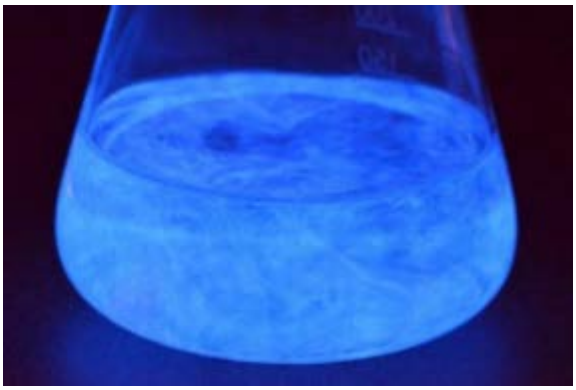

Figure 2.2: Chemiluminescence after a reaction of Hydrogen peroxide and luminol [10]

2.3.3 Mechanoluminescence

The process of light emission from a nanomaterial under the action of pressure is known as mechanoluminescence [37]. It may have further three subtypes depending on the type of external force applied.

(i) *Fractoluminescence*: Luminescence generated in some materials because of the breaking of bonds due to fractures [38].

(ii) *Piezoluminescence*: Light is produced by certain solids under pressure and this process of emission of light is known as piezoluminescence [39].

(iii) *Triboluminescence*: Emission of light due to scratching, crushing or rubbing of some materials, is known as triboluminescence [40]

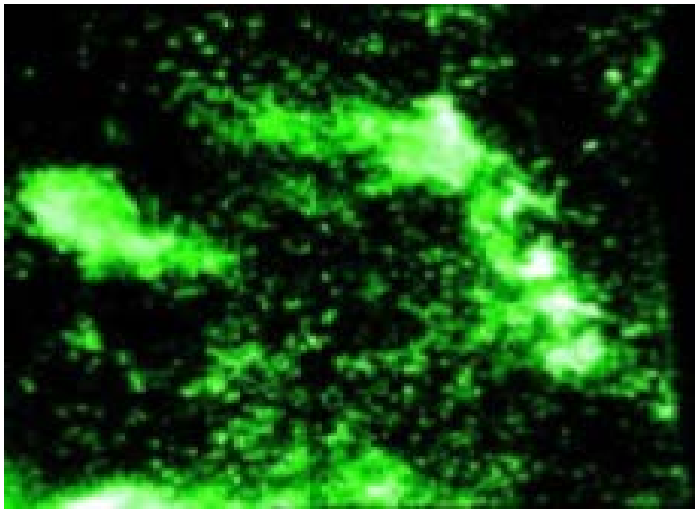

Figure 2.3: The Mechanoluminescence [41]

2.3.4 Thermoluminescence

Luminescence that arises on melting a substance which usually happens beneath incandescence, is called thermoluminescence [42]. Thermoluminescence is an

essential approach for authenticating some ancient items [43]. Assume that a substance emits both thermoluminescent and incandescent light at a certain temperature. The temporary light emission is referred to as thermoluminescence, while the continuous light emission is known as incandescence [44]. Thermoluminescent phosphors centre for trapping electron or holes in addition to luminescent centres [5]. Electrons escape from these traps upon heating and go to the luminescent centre for recombination. Energy liberated during the recombination process excites the luminescent centre and emits light [45]. Thermoluminescence is a form of luminescence, and Figure 2.4 illustrates some various examples of this phenomenon

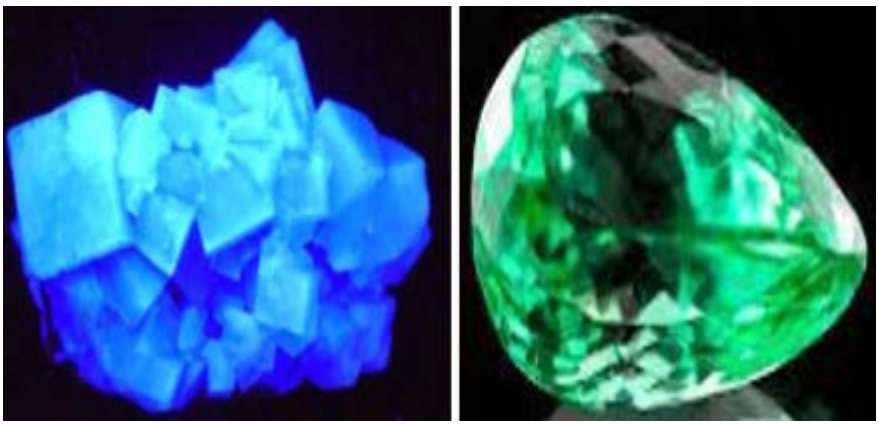

Figure 2.4: The Thermoluminescence [46]

2.3.5 Radioluminescence

Radiation emission occurs when ionized electromagnetic fields such as gamma and x-rays strike a substance, causing it to release light [47].When materials are exposed to radiation, the electrons within them become excited and migrate to higher energy levels. As these electrons return to their original states they emit light [48]. Hence, the luminescence generated is known as radioluminescence. The main applications are radioluminescence paints used in watches, compass dials, gunsights, aircraft flight instruments etc [49]. Pierre and Marie Curie were the very first people to discover radioluminescence.

Figure 2.5: The Radioluminescence [50]

2.3.6 Sonoluminescence

When droplets in a liquid are excited by sound, they release brief flashes of light. It has no practical implication yet, and thus was not in much attention but produced lots of interest in 1989 when a constant bubble is created that produce intense light in very short bursts [51].

Figure 2.6: The Sonoluminescence [51]

2.4 Traps and phosphorescence

2.4.1 Trap processes

In contrast to the band levels, which span the entire crystalline material, the trap levels are confined to a tiny volume about the trap prospective [52]. When an electron is confined to a trap, its wave function might extend over a large distance, similar to the wave functions of other electrons [53]. This confinement reduces the likelihood of the electron changing its position. Such properties are typical of a deep trap potential [54]. Shallow traps exhibit a significant variation in location, resulting in a low level of predictability in force. It is possible for discrete trap potential to be formed as a result of the material's defects, surface-related states, or even self-trapped states [55]. Some imperfections: Significant structural irregularities such as defect structures, dislocations, or grain boundaries belong to a separate category, distinct from point

defects resulting from impurities. Given that nanostructured substances possess a significant amount of exposed surface area relative to their overall volume, it is logical to conclude that surface characteristics play a significant role in determining their spectral properties. The energy gap of the materials include the surface-related states [27].

A charge trapped within a dielectric matrix induces a dielectric polarization due to the Coulomb field between the charge and the matrix. A reaction field is then generated at the site of the charge by the polarized environment. The charge is stabilized in the dielectric matrix due to its interaction with this reaction field. This is an example of self-trapping. Self-trapped levels are being utilized to clarify this occurrence in size-quantized phenomena. The charged particles are believed to be trapped in different states localized at the interface between the quantum dot and the matrix [55]. The entrapment of carriers inside the surrounding matrix, such as polymers, is crucial for the significance of self-trapped states. When polymers are injected with charges, localized acceptor states are created [56]. The distinguishing characteristics of these acceptor states include relaxations of the atomic particles and electrons in the molecular moiety wherein the electrical charge is contained and in the outside polymer matrix that surrounds it [57]. However, a neutral polymer does not naturally exist in such situations of low energy. The extent of the neighborhood's potential perturbations and the relationship of the electron/hole wave function concerning trapping potential are key factors affecting localization and entrapment. Since this trapping mechanism limits the degree of overlap of the electron/hole wave function, coupling duration is prolonged [58].

2.5 Applications of Phosphors

The cathode ray tubes, fluorescent lamps, display systems like plasma and field-emitted screens, solid-state lights, lasers, scintillators, nuclear health care, gamma ray and thermal neutron observing, etc. All use phosphors in some capacity [59]. In these contexts, phosphor substances designed around aluminate lattice structures are commonly employed.

2.5.1 Cathode Ray Tube

Images are displayed on a glowing screen within a vacuum tube known as a cathode ray tube. Images are generated by modulating, speeding up, and deflecting electron

beams in cathode ray tubes. These can double as digital notepads if need be. The phosphor used in a CRT determines how the image is displayed in terms of colour and luminosity as shown in table 2.2. Many different aluminate materials have been produced for usage in CRTs, with the cerium (III) doped $Y_3Al_5O_{12}$ material being instrumental [60]. Powdered cerium-doped lutetium-oxyorthosilicate phosphor was analyzed for use in cathode ray tubes [61].

Table 2.*2*: Phosphors used in cathode ray tubes [59]

Type of lattice	chemical composition	Colour
Oxide	ZnO:Zn	Blue-green
Oxy-sulfide	Gd_2O_2S:Tb	Yellow-green
Oxy-sulfide	Zn_2SiO_4:Mn^{2+}	Green
Borate	$InBO_3$:Eu	Yellow
Sulfide	ZnS:Ag	Blue

2.5.2 Liquid crystal displays

Liquid Crystal Displays (LCDs) is a form of flat panel display that make use of liquid crystals' natural ability to adjust light. When used to create monochromatic photos, liquid crystals rely on back light rather than direct emission of light. In 1888, Friedrich Reinitzer was the one who made the initial discovery. Screens like these can be seen in many different places, from indoor to public billboards to laptop screens, digital cameras to Tvs, smartwatches, calculators to aircraft cockpit screens [62]. The earliest LCDs were made as experiments in 1968 [63]. Since the LCD panel uses less electricity, it can be used in portable devices that run on batteries. LCDs are now common-place and essential in every aspect of our lives. Low-cost and high-resolution-density LCDs.

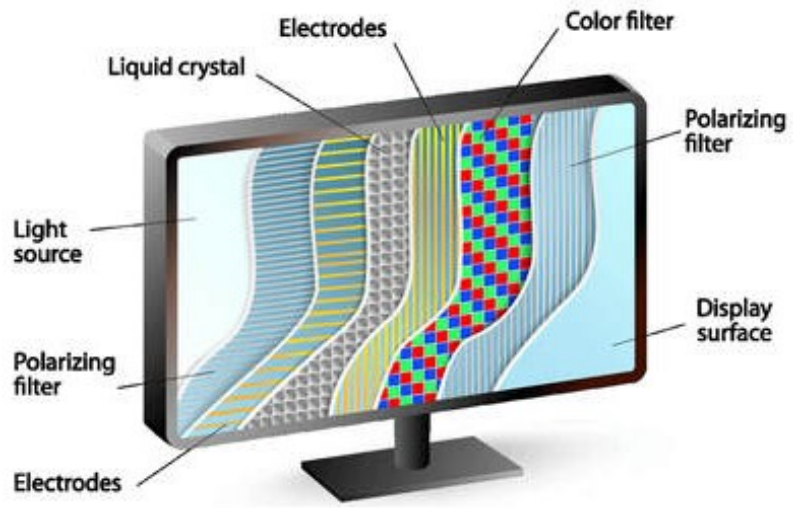

Figure 2.7: Liquid Crystal Displays [64]

2.5.3 Light emitting diodes

Electroluminescent equipment with Light emitting diodes (LEDs) can last more time, use less power, and be more efficient. LEDs are the most widely utilized semiconductor diodes currently available. It's a p-n junction diode, also known as a two-lead semiconductor diode, which glows when a charge passes. Europium (III)-doped $BaLn_2AlO_5$ (Ln = Y, Gd, and La) is widely used in state-of-the-art lighting systems because of its tunable coluor [65]. LEDs may have their emission patterns manipulated thanks to the embedded optical components that make them so tiny. When a voltage traverses an organic substance, light is created [37]. This new type of LED is called an organic LED display. Calculators, cellphones, photographs, signals for traffic, multimeters, microprocessors, camera flashes, etc. might all benefit from their quick speed and high quickness of response [65].

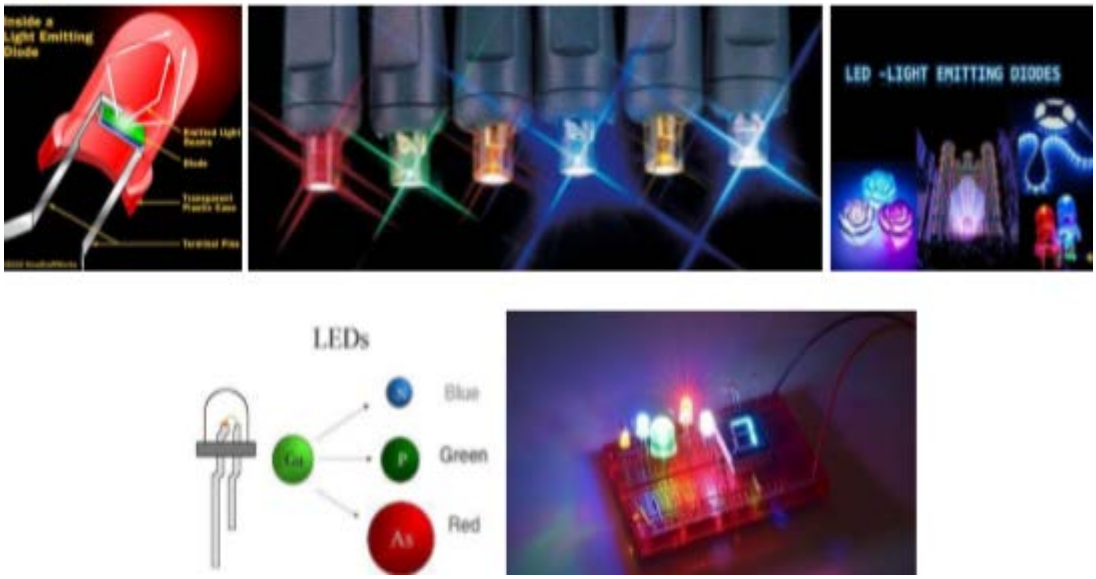

Figure 2.8: Light Emitting Diodes [65]

2.5.4 Field emission displays

The FED display functions similarly to that of a cathode ray tube, which makes use of a high voltage of approximately 10 kilovolts to accelerate electrons in order to excite phosphor [66]. The sole distinction between the two is that CRTs only have a single electron gun, but FEDs have an entire grid full of electron guns. The FEDs is a form of flat screen projection modern innovation. This display creates a color image in a vast field by having stream of electrons from the cathode emission sources impact luminescent nanomaterial [67]. Emissive and non-emissive types of technology are utilized in producing flat panel displays.

2.5.5 Vacuum fluorescent displays

Vacuum luminescent screens are similar to cathode ray tubes but require much lower voltages. In-car stereos, microwaves, and VCRs all employ these types of screens. A plasma tube serves as the anode in this setup, making it a cathode-based light source. It shines a very contrasting light in a variety of shades. Vacuum luminescent screens, or VFDs for short, are a hybrid technology that uses the best features of LEDs and LCDs. These can show digits, phrases, or letters.

Figure 2.9: Vacuum Fluorescent Display Devices [68]

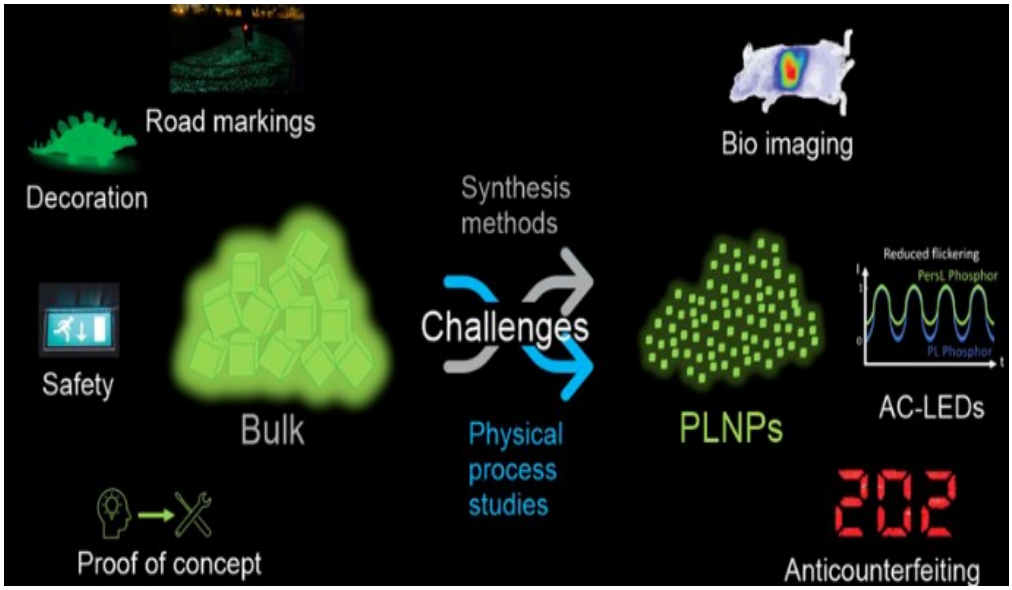

Figure 2.10: Schematic representation of persistent phosphors and their potential applications in different fields [69].

2.6 Synthesis of $SrAl_2O_4$ nanocrystalline phosphors

2.6.1 Solid State Methods

This approach is the most common method of preparing alkaline aluminate phosphors [70]. The method was first used by Matsuzawa *et al*., 1996 [71] to prepare the first afterglow luminescence phosphor ($SrAl_2O_4:Eu^{2+},Dy^{3+}$).The starting chemicals are a combination of the strontium carbonate, aluminium carbonate and the dopants. Various grinding methods are commonly used to combine these raw ingredients. In a reducing environment, these blended precursor mixtures are then sintered at high temperatures, often above 1900°C without a flux. The range of the calcination temperature is commonly reduced to between 1300 and 1500°C whenever boric acid is introduced to the process [72]. The finished product is a dense sintered mass that must be thoroughly grounded into powder.

Numerous drawbacks are inherent to this approach. The particle size variation and clumping are increased at higher furnace temperatures required for the preparation of $SrAl_2O_4:Eu^{2+},Dy^{3+}$. This leads to the formation of relatively large particles in the micron range, which negatively affects the photoluminescence performance. Rao 2012 [73] also demonstrated that additional surface deflects are created during the ball milling process, considerably lowering the photoluminescence efficiency. Poor dopant ion homogeneity also results in poor charge transfer processes because particle size and shape cannot be controlled[3].

Due to these limitations, the solid state approach is ineffective for producing $SrAl_2O_4:Eu^{2+},Dy^{3+}$. Furthermore, continued development of the persistence afterglow features and their application in an expanding range of scientific domains are hindered by the extremely high temperature and the difficulty of accurately regulating the numerous imperfections.

2.6.2 Combustion Synthesis

To counteract the negative consequences of solid-state synthesis, combustion synthesis has established itself as an accepted substitute synthetic route. During combustion-based synthesis, precursors for the host material are combined with dopant ions, most frequently oxides and nitrate salts, in an liquid mixture [8]. A quantity of combustion substance, or "fuel," such as urea or glycine, is added to this solution. The combustion reaction subsequently takes place in a furnace where the aqueous mixture is heated at a synthesis temperature between 500 and 700 °C. The response happens quickly in less than 10 minutes and results in a large, low-density material that must be grounded to produce a powdered product. Although furnace temperatures are moderate, flames can immediately reach up to 1500°C throughout the firing procedure. Comparing the combustion method to the solid-state approach, the latter takes less time and yields a more homogeneous product. As a result, it has successfully resulted in nanocrystalline $SrAl_2O_4:Eu^{2+}$, Dy^{3+} nanoscale. However, there is still no approach of regulating the amount and morphology of the particles that accumulate in the final product [4].

Additionally, even though this procedure doesn't involve ball milling, it still consists in grinding the resulting mass into its ultimate powdery state, which could introduce defects. The temperatures produced by the combustion, which can reach unmanageable flame temperatures of up to 1500°C, are often higher than those produced by conventional synthetic processes. Numerous poisonous gases, such as ammonia, carbon IV oxides and hydrides of $–CN_3$, are also produced during combustion synthesis, which is harmful when used as a bulk synthesis method to create strontium aluminate phosphors [74]. Despite high localized temperatures, incredibly crystalline powders are rarely produced by combustion because of its quick rate and the low temperatures needed to start it. To get throughout this, the photoluminescent powdery product need to be extensively annealed at temperatures between 1100-1300°C in an inert environment [61].

2.6.3 Spray pyrolysis

The nanoscale aluminate powder, chlorosilicates and sub-micron luminous nanomaterials are all synthesized using spray pyrolysis, which is one of the most popular, low-cost, easy and adaptable methods [75]. Substances with nanoscale and sub-micron sizes of particles that do not agglomerate are produced by this procedure which is a constant and one-step method. Aerosol and flame spray pyrolysis are two types of spray pyrolysis that can be used to create phosphor materials. Ultrasonic spray pyrolysis has been improved upon to create FSP (Flame Spray Pyrolysis) [76]. This is a four-step process that is utilized in the production of various materials. In the first stage, drops are formed from the precursor, and as they evaporate, they become smaller. The precursors are being converted into oxides, which will ultimately lead to the production of solid products. To remove the aerosol, a vacuum pump is also used. In the end, a fibre filter was utilized to catch the dust.

Subsequent modifications to the aluminate synthesis method included preheating the precursor aerosols in a low-temperature furnace to evaporate the solvent before introducing them to a high-temperature furnace, where they would be decomposed. Products are exceedingly pure and uniform, and their chemical composition and morphology are well controlled. However, the hollowness and porosity of products produced using the extensive spray pyrolysis technique are significant drawbacks. Their lack of solidity or permeability considerably affects. An artificial colloidal

solution is proposed for a modified spray pyrolysis technique to address the absence of a suitable substance [77].

2.7 Existing nanomaterials in Strontium Aluminate

2.7.1 A phosphor with Blue emission containing $Sr_4Al_{14}O_{25}$ Eu^{2+},Dy^{3+}

Despite the excellent quantum efficiency and blue emission centering at 480nm reported by Smets *et al*, 2005 [50], sustained luminescence was not detected in $Sr_4Al_{14}O_{25}:Eu^{2+},Dy^{3+}$ $CaAl_2O_4:Ce^{3+},Nd^{3+}$ was the first material to demonstrate blue luminescence in the UV range. Nevertheless, the long-lasting time of the phosphor exhibited rapid decline and a poor level of light productivity. Many scientists quickly began synthesizing $Sr_4Al_{14}O_{25}:Eu^{2+},Dy^{3+}$and in time,. Lin et al, 2000 [78], observed unusual emission of light at a wavelength of 494nm in a phosphor called $Sr_4Al_{14}O_{25}:Eu^{2+},Dy^{3+}$ that was produced using ceramics.

The emission also exhibited a fast start decrease in intensity. Since solid state and combustion synthesis are the only methods capable of producing highly crystalline $Sr_4Al_{14}O_{25}:Eu^{2+},Dy^{3+}$ synthetic methods have been restricted to these methods. Surface flaws and poor geometry are just two of the many issues with photoluminescence that are exacerbated by the solid state and combustion synthesis processes, as discussed earlier. $Sr_4Al_{14}O_{25}:Eu^{2+},Dy^{3+}$ particles have a low photoluminescent efficiency due to their short persistence lifespan, and no other synthetic approach has been able to efficiently overcome these faults and increase the particle's photoluminescent performance.

2.7.2 Green Emitting $SrAl_2O_4:Eu^{2+},Dy^{3+}$

The chemical compound $SrAl_2O_4$ doped with Eu^{2+} and Dy^{3+} ions. Phosphors that emit a green afterglow have undergone a thorough investigation due to their high quantum effectiveness at wavelengths that are most adaptable to the human eye. Research has shown that phosphors such as $Sr_4Al_{14}O_{25}:Eu^{2+},Dy^{3+}$ that emit blue light provide an improved long-lasting afterglow [79]. Since doped strontium aluminate emits within this range, it is still a great choice as a phosphor for safety measures, security devices, and emergency illumination. Since their initial synthesis by Matsuzawa *et al*,1996 [80], the conventional method for preparing these materials has involved solid-state and combustion syntheses [81]. These techniques introduce several negative performance metrics, as discussed earlier. Several synthetic methods, including sol-

gel and co-precipitation approaches, have been investigated to address these drawbacks. Although these techniques have lowered the temperatures at which calcination takes place and limited the size dispersion, their luminescence persistence periods are never as long as the ones seen with solid state and combustion synthesis.

2.7.3 Red emitting $Sr_4Al_{14}O_{25}:Eu^{2+},Dy^{3+},Cr^{3+}$phosphor

Luminescence studies have been performed on $Sr_3Al_2O_6:Eu^{2+},Dy^{3+}$based red emitting phosphors. Still, the red-emitting $Sr_3Al_2O_6:Eu^{2+},Dy^{3+}$components have shallow emit persistence features, with no reports of persistence periods beyond fifteen minutes [75]. This starkly contrasts the blue- and green-emitting on the $SrAl_2O_4$and $Sr_4Al_{14}O_{25}$ matrices. Many different host matrices and dopant ions have been tried in an effort to synthesize red permanent phosphors, such as $Y_2O_2S:Sm^{3+}$ and Pr doped $CaTiO_31_{27}$ [82]. Considering chromium has been commonly employed in luminescent nanomaterials as a dopant with a reddish luminescent center, the researchers Zhong and others synthesized $Sr_4Al_{14}O_{25}:Eu^{2+},Dy^{3+},Cr^{3+}$ via the solid-state approach to boost the persistent luminescence [83]. Doping $Sr_4Al_{14}O_{25}:Eu^{2+},Dy^{3+}$ with chromium extends the red colour's persistence for more than sixty minutes by continuously transferring energy from Eu^{2+} to Cr^{3+} as demonstrated by the combustion synthesis of $Sr_4Al_{14}O_{25}:Eu^{2+},Dy^{3+}$ by Luitel 2000 [84] .

CHAPTER THREE

MATERIALS AND METHODS

3.1 Methodology

The solution combustion method is a versatile, simple and rapid synthesis method for nanomaterials (eg, phosphor) using self-sustained reaction in homogenous solutions of various oxidizers .It has generated more interest in the field of nano-luminescence materials. The solution combustion method has been carried out using urea as fuel. It is an exothermic process that occurs with the evolution of heat. The energy needed for the combustion reaction to take place is supplied from the reaction itself hence it is called a self-propagating high-temperature synthesis. The characteristics of solution combustion reaction, to reduce power and generate gas and can be controlled by the selection of the fuel such as urea. Compared to other conventional ceramic process technique solution combustion method has shown advantages of taking few minutes to complete the reaction and the equipment processing are inexpensive

Non-destructive characterization methods and the combination procedure employed in the present investigation are briefly described in this section. The alkaline earth aluminate phosphor powders were made using a combustion process.

3.2 Materials

In this study aluminium nitrate and strontium nitrate were used as the starting chemicals. Europium nitrate and dysprosium nitrate was used as luminescent centres and trap centres, boric acid was used as flux agent and urea as a fuel. All starting materials are of analytical grade as shown in table 3.1.

Table 3.1: Summary table for Chemicals used to prepare $SrAl_2O_4:Eu^{2+},Dy^{3+}$

Compound	Source	Purity
Strontium nitrate	Kobian scientific chemicals	99.9%
Aluminium nitrate nanohydrate	Alfa Aesar, Karlsruhe	≥98.5%
Dysprosium nitrate pentahydrate	Alfa Aesar, Karlsruhe	99.9%
Boric acid	Kobian scientific chemicals	99%
Urea	Kobian scientific chemicals	≥99.9%
Europium nitrate hexahydrate	Alfa Aesar, Karlsruhe	99.9%

3.3 Experimental procedure

$SrAl_2O_4:Eu^{2+}$, Dy^{3+} phosphors were synthesized using the solution - combustion method. The starting raw materials used in the experiment include various proportions of analytical pure grade $Sr(NO_3)_2$,$Al(NO_3)_3{\cdot}9H_2O$,$Eu(NO_3)_3{\cdot}6H_2O$ and $(Dy(NO_3)_3{\cdot}5H_2O$ urea (CH_4N_2O) and boric acid (H_3BO_3). The raw materials were weighed according to the chemical composition of $SrAl_2O_4:Eu^{2+}$, Dy^3, dissolved in 10 ml of de-ionized water and thoroughly mixed using a magnetic stirrer for 15 minutes without heating to obtain a uniform solution. In the first group, six samples were prepared to study the influence growth temperature of variation. on the structural and optical properties of the $SrAl_2O_4:Eu^{2+}$, Dy^{3+} phosphor. The second set consist of four samples used to study the influence of variation host material and the Al concentration was kept constant at 1 mol% for all the prepared solutions. This was combined with varying concentrations; 1, 1.5, 2, and 2.5 mol% of Sr were taken. The third set consist of five samples used to study the influence of variation of co-dopants, Dy^{3+} molar ratio on the structural and optical properties of the $SrAl_2O_4:Eu^{2+}$, Dy^{3+} phosphor. The samples were mixed in the mass ratios 0.1, 0.2, 0.4, 0.6 and 0.8 mol%. The solutions were then poured into China crucibles and placed one at a time in a muffle furnace pre-heated at 500℃. Combustion time was 5–6 min per sample. White voluminous foam was obtained by combusting the mixture at temperatures of 500–1000°C. Initially, the solution boiled and underwent dehydration, followed by decomposition releasing large amounts of gases (oxides of carbon, nitrogen and ammonia). The voluminous foam was milled to obtain the fine, white powders. The powders were stored in transparent sample glass bottles for characterization.

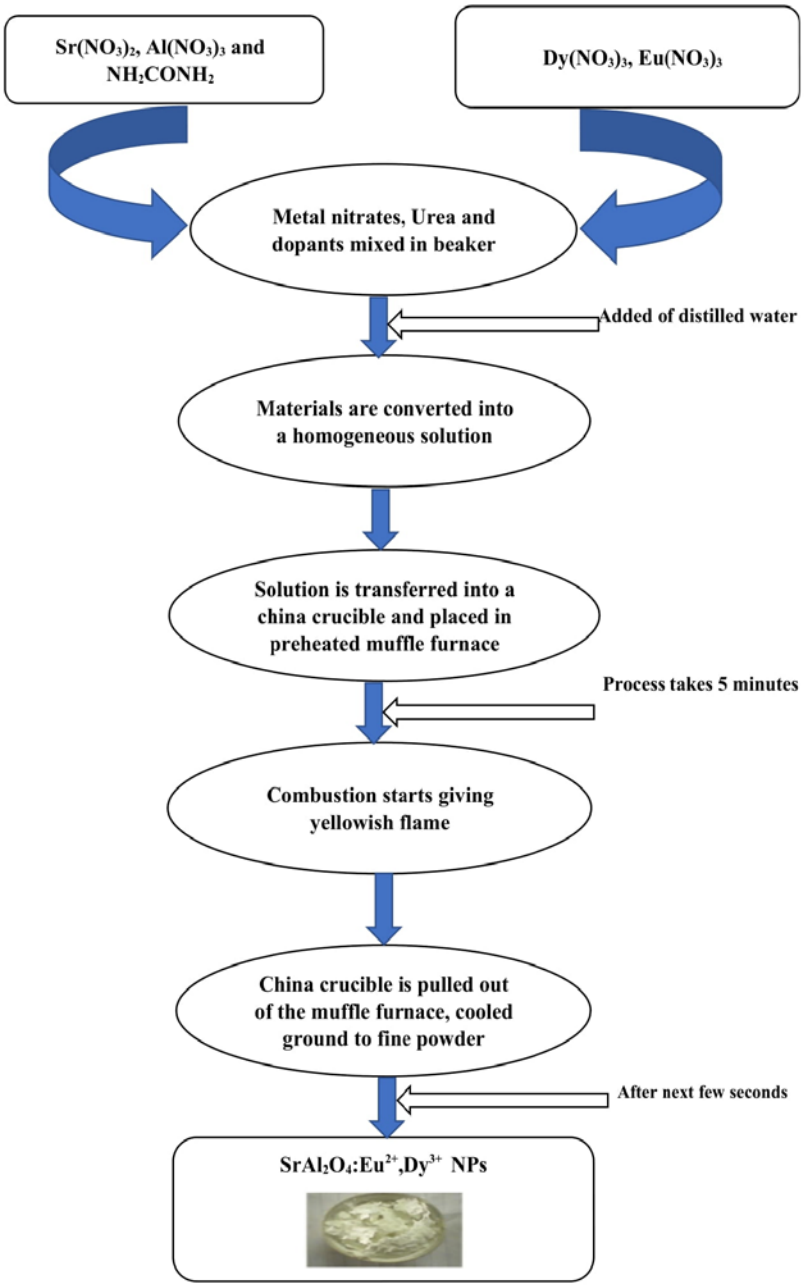

Figure 3.1: A diagram illustrating the procedure of preparing Strontium aluminate phosphor

3.4 Characterization

3.4.1 XRD Study

X-ray diffraction (XRD) is a powerful non-destructive technique used to investigate structural properties of crystalline materials. It can be used in application such as phase identification, determination of grain size, composition of solid solution, lattice constants and degree of crystallinity in the mixture of amorphous and crystalline substances. Every crystalline substance possesses a distinct atomic configuration which is determined by the characteristics of its unit cell. XRD is the scientific method utilized to determine the spatial placement of atoms in a material through looking at the scattering of X-rays by the crystal's particles[24].XRD is a highly adaptable non-destructive approach employed for investigating the overall composition of solid nanomaterials in large quantities. It allows for the determination of crystallite size, stress phase identification, lattice constants, analysis of single crystal orientation, examination of polycrystalline orientation, assessment of texture, and determination of film thickness, among other applications. XRD examination may study the level of crystalline defects and identify the main crystallographic planes of a specific material[27]. The target materials that are usually used are Cu, Co, Mo and Cr. Each of these has specific characteristic wavelengths[85] as shown in table 3.2.

Table 3.2: List of elements commonly used as metal targets in XRD.

Elements used	Wavelength in nm
Cu	0.15418
Cr	2.2902
Co	0.17902
Mo	0.7107

Bragg's Law

The X-ray diffraction (XRD) concept is closely connected to Bragg's law. Crystal exhibit a phenomenon where the atoms within them are affected by X-rays, resulting in the occurrence of entanglement. The interactions can be viewed as the atomic particles within a crystal structure reflecting the vibrations. Since a crystal structure consists of a well-organized collection of atoms, the reflections occur from the atomic

planes. Visualize a concentrated beam of X-rays with a uniform wavelength passing through a crystal, in which one of its surfaces is inclined at an angle of θ in relation to the incoming ray. The ultraviolet radiation interacts with a crystal and is scattered by the particles in adjacent surfaces. Figure 3.2 depicts two X-rays that demonstrate the separation between atomic planes at a specific distance known as "d".

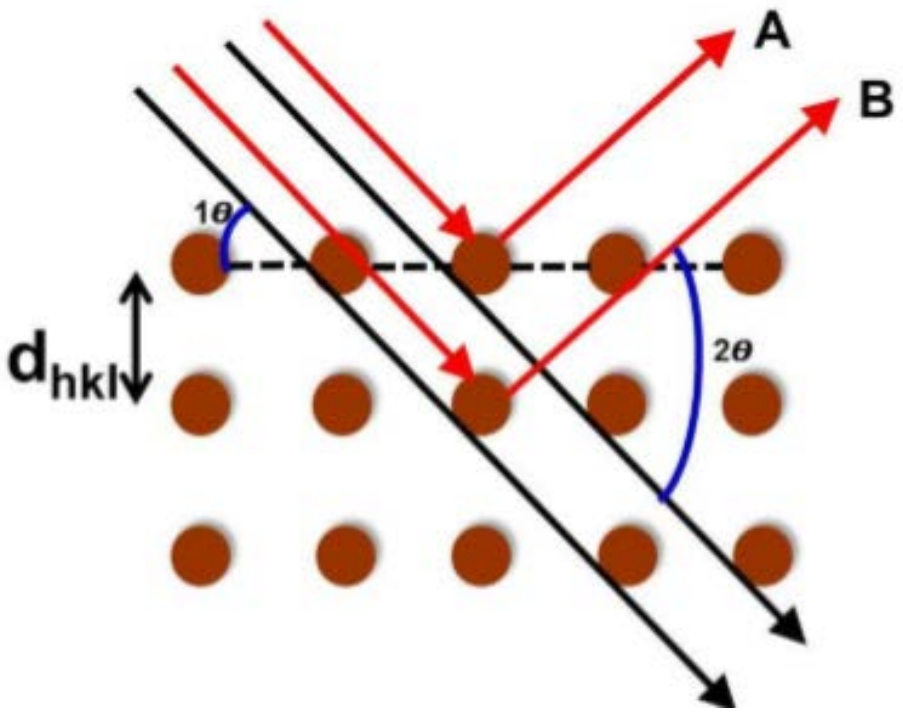

Figure 3.2: Formation of Bragg's diffraction [86]

Ray A undergoes reflection when it strikes the uppermost crystalline surface at an angle θ that is identical to the angle in coming ray. In a comparable manner Ray B undergoes reflection on the bottom part at the equivalent angle θ. During Ray B's time inside the crystal, it covers a distance that is 2α units longer than the distance covered by Ray A. Assuming the distance 2α is equivalent to a whole number of wavelengths (nλ), then Rays A and B will be in phase as they escape the crystal, resulting in constructive interference. When the distance 2α is not a whole number of wavelengths, then destructive interference will take place, resulting in a decrease in the strength of the waves compared to their initial state upon entering the crystal. Hence, the requirement for constructive interference to happen is that the product of the wavelength (λ) and the integer value (n) is equal to twice the distance 2α .

However, utilizing trigonometry, the precise value of the distance 2a in relation to the spacing, d, across the atomic surface.

$$a = dsin\theta, or\ 2a = 2dsin\theta \qquad \text{thus}$$

$$n\,\lambda = 2dsin\theta \qquad (1)$$

The XRD technique is employed for the analysis of structural characteristics, including crystallite size, microstrain (stress), texture coefficient, and dislocation density (δ). Prior to their technological uses, it is crucial to possess understanding of the specific parameters, particularly for novel materials. Furthermore, the XRD is the most convenient instrument for doing crystallographic structural analysis, including tasks such as identifying phases, quantifying phases, and refining lattice parameters.

3.4.2 Crystallite size measurement

The existence of certain types of defects including edge dislocations, can alter the arrangement and intensities of diffraction peaks in structures that have diameters on the millimeter scale. The small size of grains is occasionally considered as an extra type of dislocation that has the ability to change the widths of diffraction peaks[61]. Peak broadening occurs due to the existence of tiny particles. The determination of crystallite size can be easily calculated using Scherrer's formula [79] which considers the peak width (expressed as the full-width at half maximum peak intensity, or FWHM), peak position, and wavelength.

$$D = \frac{K\lambda}{\beta COS\theta} \qquad (2)$$

The variables utilized in the equation are as follows: K represents the form factor with a value of 0.9, D represents the size of the crystallite particle, λ represents the wavelength of the incident X-ray beam (0.15405 nm), θ represents the Bragg's diffraction angle, and ß represents the whole width at half-maximum in radians. The Scherrer's formula is frequently employed for determining the dimensions of extremely small crystals based on the determined width of their diffraction patterns. It should be noted that the choice between using a value of K = 0.9 or 1 is subject to the expected morphologies of the crystallites in the sample [54].

3.4.3 Determination of lattice parameters

In the monoclinic phase, the interplanar distance of the plane is determined by the lattice parameters *a,b* and *c*, as well as the Miller indices *hkl* [48].

$$\frac{1}{d^2_{(hkl)}} = \frac{4}{3}\left(\frac{h^2 + hk + k^2}{a^2}\right) + \frac{l^2}{c^2} \qquad (3)$$

The amount of distance between planes with Miller indices *h*, *k*, and *l* is denoted by d, whereas the lattice parameters are represented by *a*, *b* and *c*. The lattice constant *a* for a given plane was determined by using equation (4).

$$a = \frac{\lambda}{\sqrt{3}sin\theta} \qquad (4)$$

3.5 Fourier Transform Infrared Spectroscopy

The infrared absorption spectrum of solids, liquids, and gases can be recorded with FT-IR since it is a simple, molecular, and non-destructive spectroscopic approach [87]. FT-IR can identify unknown materials, it can determine the quality or consistency of a sample and it can determine the amount of components in a mixture. The vibrational frequencies of a molecule can be calculated from its absorption spectrum, providing insight on the molecule's structure and chemical bonding. Recording a material's spectrum using a method called Fourier transform infrared spectroscopy allows researchers to detect the presence or absence of distinct species [24]. This tool can be used on both organic and inorganic samples, and its affordable. Broadband spectra from the near IR (12800–4000 cm^{-1}) to the far IR (50–1000 cm^{-1}) are acquired with a Fourier transform infrared spectrometer, a type of spectrometer that dates back to the third generation [86].

The Basic Idea Passing infrared radiation through a sample and measuring the amount absorbed and transmitted is what Fourier transform infrared spectroscopy is all about. A material's unique fingerprint can be seen in its absorption and transmission spectra. The infrared absorption spectrum shows evidence of both stretching and bending vibrations. When a molecule's vibration causes a shift in its electric dipole moment, it shows up as a peak in the infrared [49]. Homonuclear diatomic molecules (O_2, N_2, and Br_2) do not absorb infrared because their stretching vibrations do not cause a change in dipole moment. When stretched or squeezed, the link in CO and IBr

changes its dipole moment and produces an infrared spectrum. Analyzing the energy absorbed by a molecule as it passes through phases between atomic groups can shed light on the types of atoms bonded or clustered in an otherwise mysterious substance. Spectral location can be written as a function of the wavenumber in units of cm^{-1}. Transmittance (T) and absorbance (A) are two different ways of expressing the strength of a band. The transmittance (T) and wavenumber (cm^{-1}) of an FT-IR spectrum are typically plotted. The band between 4000 and 400 cm^{-1} is the most important part of the infrared spectrum. The absorption peaks for the inorganic phosphor materials was synthesized and characterized in the range of 1500-400cm^{-1}.

The size of the peaks in the spectrum is a direct indication of the amount of material present. Fourier transform infrared spectroscopy is preferred over dispersive or filter methods of infrared spectral analysis for several reasons:

• It is a non-destructive technique

• It provides a precise measurement method which requires no external calibration

• It can increase speed, collecting a scan every second

• It can increase sensitivity – one second scans can be co-added together to ratio out random noise

• It has greater optical throughput

• It is mechanically simple with only one moving part

Since FT-IR equipment include an inherent wavelength calibration standard—a Helium-Neon laser—no user calibration is required. Because of their mechanical simplicity, these instruments rarely experience malfunctions. Phosphor material structure and bonding have been analyzed by recording Fourier transform infrared spectra from 4000 to 400 cm-1 using KBr pellets and a Nicolet iS50 FT-IR spectrophotometer [88].

3.5.1 UV-Visible Spectra Measurement

Absorption spectroscopy performed in the ultraviolet-visible range is known as UV-Vis spectroscopy, UV-Vis spectrophotometry, or simply UV-Vis. This means that it employs light within the visible spectrum and its nearby regions (near ultraviolet (UV) and near infrared (NIR)). Transition metal ion and highly conjugated organic compound solutions can have their absorber concentrations quantitatively determined

using a UV-Vis spectrophotometer. The spectra were captured from two hundred to seven hundred nm [89]. The Beer-Lambert formula states that the efficiency of a solution's absorption varies according to the quantity of the substance that absorbs present in the solution and the distance of the path taken. Consequently, the absorber concentration in a solution can be calculated using UV-Vis for a given route length. The absorbance shifts as concentration increases. This can be approximated from a calibration curve or computed explicitly from a reference (tables of molar extinction coefficients).

Two beams, one for the sample and one for the standard, are typical in UV-Visible spectrometers. Absorbance versus wavelength is plotted using a UV-Visible spectrum device. The 200-700 nm range is a common place to plot UV-visible spectra. An atomic cluster known as a chromophore only absorbs light in a particular region of the UV-vis spectra[12]. When figuring out the optical characteristics of nanomaterials (which include things like the bandgap or energy difference), optical absorption is a crucial parameter to investigate.

Figure 3.3: UV Visible spectrometer at Pwani University analytical laboratory.

CHAPTER FOUR

RESULTS AND DISCUSSION

4.1 Influence of synthesis temperature on the structural and optical Properties of the $SrAl_2O_4:Eu^{2+},Dy^{3+}$ Phosphors.

4.1.1 Experimental Procedure

The powder phosphors were prepared by a combustion method at different initiating temperatures ranging from 500–1000℃.The following precursors: $Sr(NO_3)_2$,$Al(NO_3)_3{\cdot}9H_2O$,$Eu(NO_3)_3{\cdot}6H_2O$ and ($Dy(NO_3)_3{\cdot}5H_2O$ urea (CH_4N_2O) and boric acid (H_3BO_3) all in analytical purity were weighed according to their stoichiometry to prepare the phosphor powders. Six samples were prepared to study the influence growth temperature of variation on the structural and optical properties of the $SrAl_2O_4:Eu^{2+}$, Dy^{3+} phosphor. The solutions were then poured into China crucibles and placed one at a time in a muffle furnace pre-heated at 500℃. Combustion time was 5–6 min per sample. White voluminous foam was obtained by combusting the mixture at temperatures of 500–1000℃. Initially, the solution boiled and underwent dehydration, followed by decomposition releasing large amounts of gases (oxides of carbon, nitrogen and ammonia). The voluminous foam was milled to obtain the fine, white powders. The powders were stored in transparent sample glass bottles for characterization.

4.1.2 X-Ray Diffraction Analysis

XRD is an efficient analytical technique used for identification of structural properties of crystalline materials. It is also used for identification of phases, determination of crystallite size, lattice constants, and degree of crystallinity in a mixture of amorphous and crystalline materials. In this study Rigaku miniFlex was used to study the structural properties of the prepared phosphor. The XRD profiles of the synthesized phosphor are depicted in the Figure 4.1. XRD patterns shows that the samples calcined at T= 500-600 ℃ have monoclinic phase with some impurities of $SrAl_2O_4:Eu^{2+}$, Dy^{3+} nanoparticles with a dominance of monoclinic phase. As the furnace temperature rose to 700 ℃, the monoclinic phase becomes dominant. At furnace temperature 800 ℃ and 1000 ℃ , the monoclinic phase disappears and the samples show hexagonal phase.

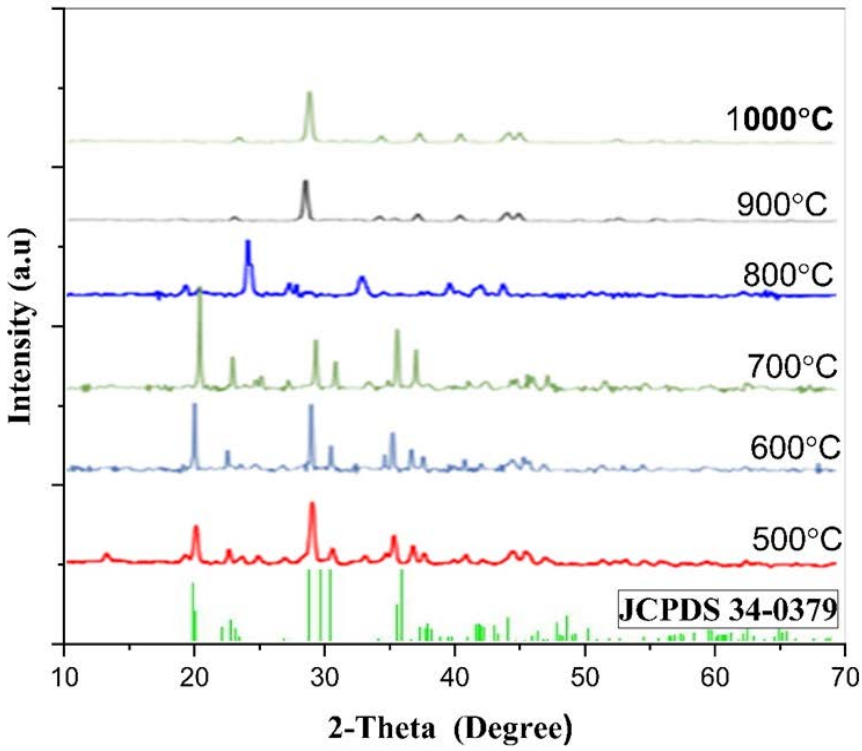

Figure 4.1:XRD profiles of strontium aluminate prepared at varying furnace temperatures.

Five prominent peaks at 2θ values 19.96, 28.46, 29.27, 29.98, and 35.11 degrees correspond to the crystallographic planes (0 1 1), (-2 1 1), (2 2 0), (2 1 1), and (0 3 1), respectively of the monoclinic phase, which are indicative of the $SrAl_2O_4$ crystal lattice configuration which matched well with the standard JCPDS file No. 34-0379. The synthesized samples exhibit broader and more strong peaks, which suggest a smaller crystallite size and an increase in the level of crystallinity [31]. $SrAl_2O_4:Eu^{2+}$, Dy^{3+} exhibits two distinct phases, namely a hexagonal phase (referred to as the β-phase) at high [90] temperatures and a monoclinic phase (referred to as the α-phase) at low temperatures. The XRD profiles found confirm the presence of a dominating monoclinic $SrAl_2O_4:Eu^{2+}$, Dy^{3+} phase. A crystal structure of the produced NPs was determined to be in the low-temperature monoclinic phase with space group P_{21} using VESTA software. The crystallite sizes of the samples was calculated from the most intense peak centered at 2θ values 19.96° employing the

Debye-Scherer formula[61]. The as-prepared $SrAl_2O_4$:$Eu2^+$, Dy^{3+} samples exhibited crystallite sizes ranging from 35 to 42 nm.

$$D = \frac{K\lambda}{\beta \cos\theta}$$

As defined earlier on page eqn 2. The crystallite sizes are shown on table 4.1. Consequently, it was observed that the crystallite size exhibited a significant correlation with the synthesis temperature. Enlargement in crystallite size suggests that tiny particles are diffusing and combining to produce bigger particles as the synthesis temperature increases. Furthermore, a rise in the $SrAl_2O_4$:Eu^{2+}, Dy^{3+} crystallite size upon raising the synthesis temperature supports the idea that a small crystallite size is necessary to enable the formation of a monoclinic steady crystalline structure. The lattice parameters for monoclinic and hexagonal phases did not match well with standard bulk indicating that the material is under strain(ε). The strain computation provides more details regarding the structural features of $SrAl_2O_4$:Eu^{2+}, Dy^{3+} which can be determined by applying Equation

The strain of the synthesized nanocrystalline particles begin to rise from 0.280 to 0.320 as the synthesis temperature is raised to 700 °C. However, an additional rise in the furnace temperature causes the strain to fall back to 0.243. This rise in strain is attributed to the rise in dislocation density in the $SrAl_2O_4$:Eu^{2+}, Dy^{3+} [81]. The degree of dislocation (δ) is expressed to be the length of the dislocations per unit volume of the material. The determination of dislocation density by equation 5 .

$$\delta = \frac{1}{D^2}$$

Table 4.1 presents δ and ε values for various nanostructure strontium aluminates phosphors. A notable observation is that when the values of β fall, there is a growth in the diameters of the crystallites, accompanied by a decrease in both the δ and ε values. The reduction in δ and ε serves as an indication that phosphors are undergoing a transition toward a more crystalline state.

Table 4.1: The calculated values of the structural parameters of as-prepared $SrAl_2O_4:Eu^{2+}$, Dy^{3+} at different growth temperatures.

Growth temperature	Lattice parameters, ***a*** (nm)	Strain (**ε**)	Dislocation density (**δ**) (**l**ines/m^2)	Crystallite size (D) nm
500℃	0.844	0.280	5.99×10^{-4}	40.86
600℃	0.825	0.311	7.36×10^{-4}	36.85
700℃	0.831	0.320	7.82×10^{-4}	35.74
800℃	0.828	0.260	6.64×10^{-4}	38.81
900℃	0.834	0.258	6.57×10^{-4}	39.02
1000℃	0.829	0.243	5.77×10^{-4}	41.62

4.1.3 Fourier Transform Infrared Spectroscopy

FTIR is a rapid and accurate method for the qualitative examination of materials under

study

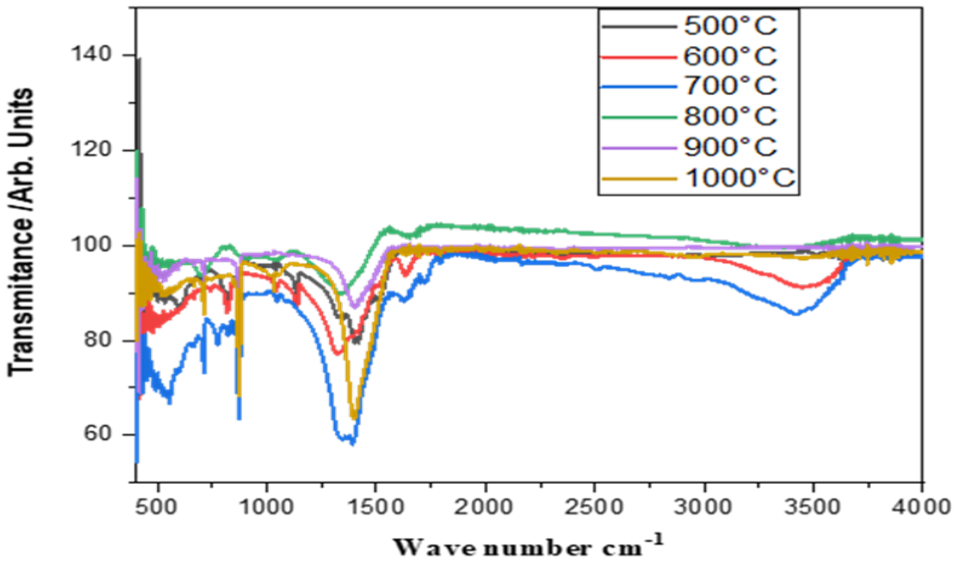

Figure 4.2: FT-IR patterns of $SrAl_2O_4:Eu^{2+}$, Dy^{3+} NPs prepared at varying furnace temperature .

The FT-IR examination is a crucial instrument for enhancing comprehension of the qualities of the acquired sample[91]. The central infrared range (4000–400 cm^{-1}) is precious for organic and inorganic substances spectroscopic analysis. Figure 4.2 displays the FTIR transmittance profile of the strontium aluminate NPs. The infrared spectra of strontium aluminate show distinct bands a prominent band at 3399 cm^{-1} and weaker bands at approximately 1800–1700 cm^{-1} associated with vibrations caused by the stretching and bending vibrations of O–H. A high level of dampness in the surroundings may result in the O–H group formation in strontium aluminate. The infrared profile spectra of strontium aluminate exhibit a prominent maximum at a wavenumber of 1482.23 cm^{-1}. The precise provenance of this summit, however, remains somewhat ambiguous. The peaks detected at this specific wavenumber cannot be ascribed to the $Sr(NO_3)_2$ compounds synthesized as precursors during fabrication.

4.1.4 UV-vis analysis

The band-gap value of various $SrAl_2O_4:Eu^{2+},Dy^{3+}$ phosphor samples was determined by recording their absorption bands in the spectrum range of 200 to 800 nm

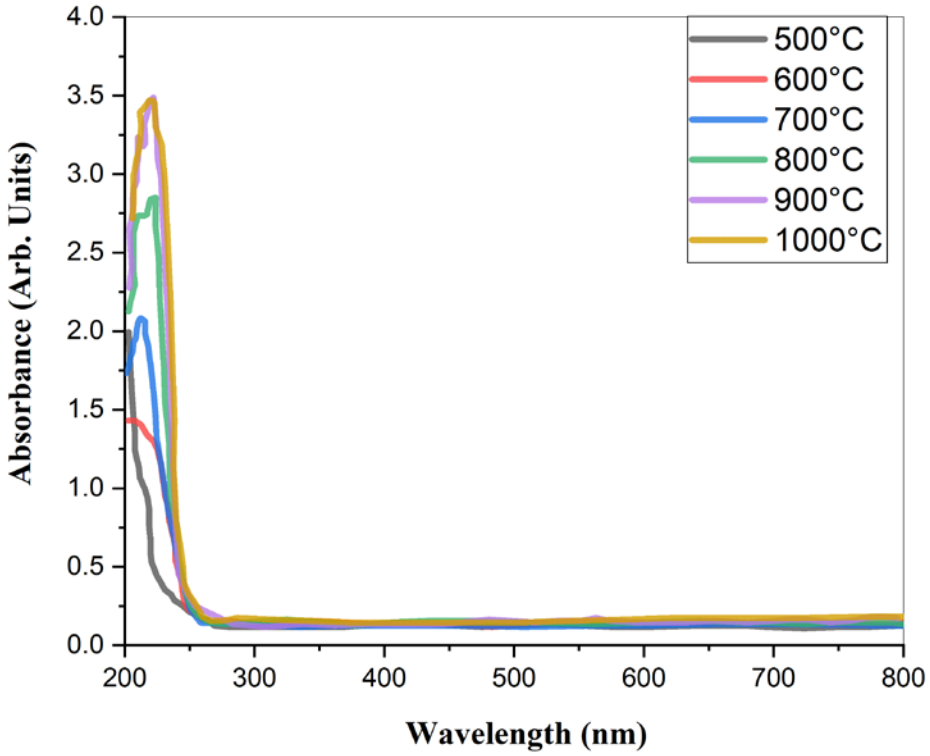

Figure 4.3: Graph showing absorbance profiles of $SrAl_2O_4:Eu^{2+}$, Dy^{3+} (SAED) synthesized at different combustion temperatures

Quantum entanglement effects can modify the band gaps of nanocrystalline particles, with the extent of the impact being determined by the size of the nanoparticles [92]. Consequently, this might impact the absorption wavelength of the generated materials. The figure 4.3 demonstrates a strong relationship between the growth temperature and the movement absorbance peaks towards longer wavelengths [78]. An increase in furnace temperature resulted in a shift of the absorption edges towards greater wavelengths. The estimated absorption edges were 240, 249, 250,251,255, and 260 nm for growth temperatures of 500, 600, 700, 800,900 and 1000 °C respectively. The Stokes shift of $SrAl_2O_4:Eu^{2+},Dy^{3+}$ nanoparticles is greater when the powders are produced in open air, mostly because of the intense phonon coupling. The noted Stoke shift was a result of the band-edge transition, which was influenced by the variation of crystal sizes [88]. The observed correlation between the Stoke shift and synthesis temperature can be explained by the accelerated nucleation process at

greater temperatures[93]. As a result, particles with a larger area of contact are formed, which facilitates a greater number of interactions between electrons and holes.

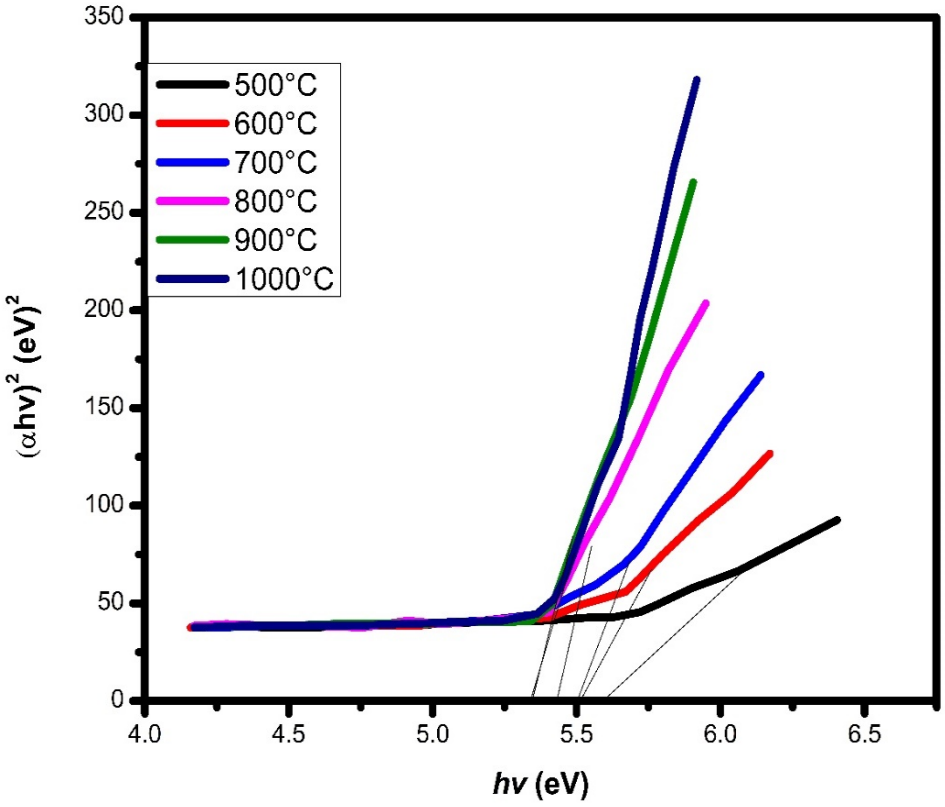

Figure 4.4: Tauc plot $(\alpha hv)^2$ against hv) to ascertain the optical energy band gap of the $SrAl_2O_4:Eu^{2+}$, Dy^{3+} phosphors

Absorbance spectra with Tauc plot, which is frequently used to determine the near band-edge optical absorption of semiconductors, were utilized to determine the optical energy band gap of SAED. Optical energy band gap of the as-prepared SAED can be determined by projecting the linear component *hv* and identifying the point where it intersects. The $SrAl_2O_4:Eu^{2+},Dy^{3+}$ compound exhibited band gap values of 5.62, 5.51,5.50, 5.49, 5.44, and 5.4 eV at furnace temperatures of 500, 600, 700, 800,900 and 1000 °C, respectively. The measured results exhibit a modest elevation compared to the documented bulk estimation of 5.5 eV. The increase in optical band gap is ascribed to the extremely small dimensions of the crystallite size and the

resulting entrapment of electronic energy in the NPs [12]. Overall NPs samples generated in the present research had a crystallite size particle size of approximately 41 nm, as determined by XRD tests. The following explains the significantly larger optical band gaps found compared to the bulk value.

Obtaining a precise measurement of Eg from experimental data is challenging in practice, mostly due to the influence of temperature and the potential presence of excitonic characteristics near the lower boundary of the conduction band. The absence of distinct attributes over the full spectrum hinders the ability to ascertain a precise figure for Eg. The materials used in this investigation possess a broad band-gap characteristic [94].

4.2 Effect of as-prepared $SrAl_2O_4:Eu^{2+},Dy^{3+}$ Nanoparticles host composition on the structural and optical properties

4.2.1 Experimental procedures

$Sr(NO_3)_2$,$Al(NO_3)_3{\cdot}9H_2O$,$Eu(NO_3)_3{\cdot}6H_2O$ and ($Dy(NO_3)_3{\cdot}5H_2O$ urea (CH_4N_2O) and boric acid (H_3BO_3) were employed as starting materials. The phosphor powders were prepared with varying amounts of $Sr(NO_3)_2$ and $Al(NO_3)_3$. The Al/Sr ratio changed from 1 to 2.5mol %. H_3BO_3 was evaluated as fluxing agent. In all recipes 0.006 mole Eu^{2+}, 0.003 mole Dy^{3+} and 0.02 mole boric acid were input to the composition. For this purpose 4 different recipes were prepared and coded as S_1 (Al/Sr: 1), S_2 (Al/Sr: 1.5), S_3 (Al/Sr: 2) and solutions were then poured into China crucibles and placed one at a time in a muffle furnace pre-heated at 700℃. Combustion time was 5–6 min per sample. White voluminous foam was obtained by combusting the mixture at temperatures of 500–1000°C. Initially, the solution boiled and underwent dehydration, followed by decomposition releasing large amounts of gases (oxides of carbon, nitrogen and ammonia). The voluminous foam was milled to obtain the fine, white powders. The powders were stored in transparent sample glass bottles for characterization.

4.2.2 X-Ray Diffraction

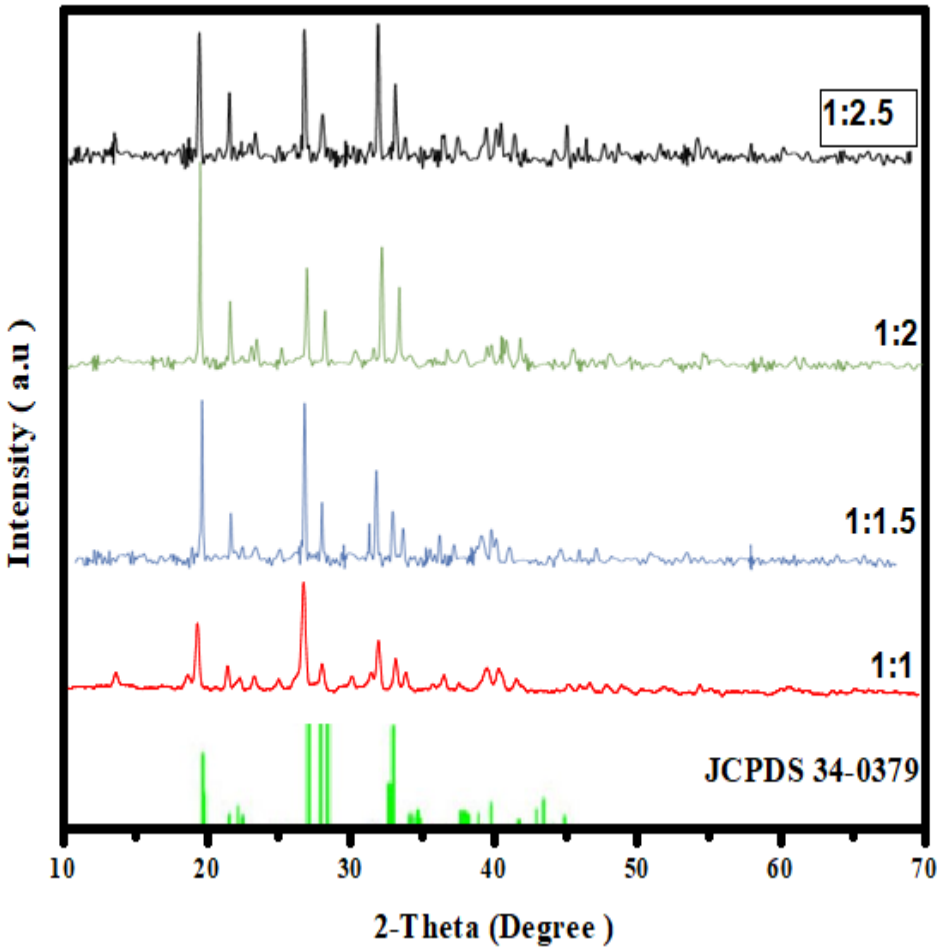

Figure 4.5*:* The X-ray diffraction of SAED were obtained using the solution combustion method at different molar ratios of Al/Sr.

Figure 4.5 shows XRD profiles for $SrAl_2O_4:Eu^{2+},Dy^{3+}$ prepared from solution combustion method at varying molar ratios of $Sr(NO_3)_2$ at 1,1.5,2,2.5. Based on the observed spectrum, it is evident that the NPs possess a polycrystalline structure, as indicated by the diffraction spectrum at $2\theta = 19.96°, 28.46°, 29.27°$ and $35.1°$ indexed as (0 1 1), (-2 1 1), (2 2 0) and (2 1 1) planes of monoclinic phase of $SrAl_2O_4:Eu^{2+},Dy^{3+}$ (JCPDS Card No. 34-0379). Analysis of these diffractive peaks reveal that 2mol% Sr favour pure monoclinic phase matching with the JCPDS data file (no. 34-0379) while higher concentrations of calcium; 2.5 mol% Sr, seem to

favour the formation of mixed phase. Weak diffraction peaks of the precursor is formed due to incomplete combustion were also observed [77].

The table 4.2 provides information about the host material used in the solution combustion approach to manufacture SAED phases. The precursors used in this process have different Al/Sr ratios.

Table 4.2: Host compounds of $SrAl_2O_4:Eu^{2+},Dy^{3+}$ synthesized at different Al/Sr ratios

Nominal Al/Sr ratio	Host material
1:1	impurities, $SrAl_2O_4$
1:1.5	$SrAl_2O_4$,impurities
1:2	$SrAl_2O_4$
1:2.5	$SrAl_2O_4$ with impurities

The Scherrer equation is employed in order to determine the crystallite size, denoted as (D) eqn(2). The broadening of the diffraction pattern was determined at half of its highest intensity, which is expressed in radians as the FWHM. The wavelength of the X-ray used is 0.15406 nm. The calculated crystallite sizes from the most intense peak at varying Sr ratios are displayed in Table 4.2. The size of the crystallites decreases significantly as the concentration of Al prepared in the initial solution rises, reaching an optimal value of 17.68 nm for the nanoparticles generated with 2 mol% Sr. The reduction in the size of the crystallites is attributed to the increased integration of aluminum ions in the strontium sites of the $SrAl_2O_4$ lattice. The reduction in crystallite size indicates a decline in the quality of the $SrAl_2O_4$ crystal structure due to the presence of aluminum, leading to an increase in the overall proportion of grain boundaries in the nanoparticles.

The strain that is present in the samples is determined using a mathematical procedure, and the outcomes of this calculation are displayed in Table 4.3. The strain's measurements exhibit a positive correlation with the content of Al, indicating a decline in the crystalline nature of the $SrAl_2O_4:Eu^{2+},Dy^{3+}$ NPs. Mallika and her colleagues showed that a rise in strain leads to a decrease in crystallite size and an improvement in peak broadening[13].

Table 4.3: Nominal ratio, FWHM, Crystallite size, strain and Lattice parametrs of $SrAl_2O_4:Eu^{2+}$, Dy^{3+}

Nominal Al/Sr ratio	FWHM	Crystallite size (nm)	Strain **(lines/m^2)**	Lattice parameter (a) (nm)
1:1	0.36	24.75	29.533	0.84470
1:1.5	0.41	21.20	33.64	0.84473
1:2	0.44	19.86	36.10	0.84477
1:2.5	0.49	17.68	40.20	0.84483

4.2.3 Fourier Transform Infrared Spectroscopy

Fourier transform infrared absorption spectrum of the material synthesized at 700 °C (Figure 4.6) exhibits strong nitrate absorption bands at approximately 1365cm^{-1}, suggesting that the breakdown of $Sr(NO_3)_2$ has not yet begun. The Al–O stretching vibration at 1630 cm^{-1} and the other vibrations associated with the AlO_4 unit at 500–900 cm^{-1} exhibit broadness caused by the low quality of the Al_2O_3 starting material. At a temperature of 700 °C , small amounts of nitrates are still present. However, the vibrations of the Al-O bonds, particularly the one at 1440 cm^{-1}, suggest the creation of the $SrAl_2O_4$ phase, while the vibrations of Al_2O_3 still remain more prominent. The Al–O vibrations exhibit complete development and a high degree of sharpness only when the host material composition is at 2mol % [95].

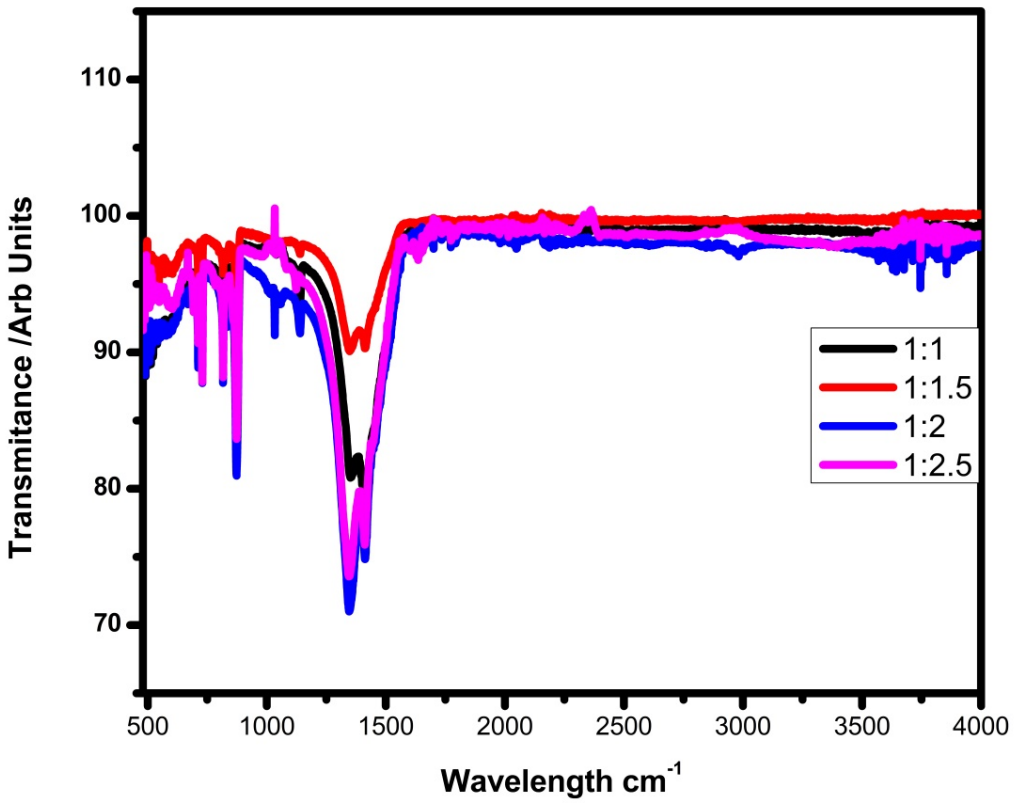

Figure 4.6: The FT-IR spectra of $SrAl_2O_4:Eu^{2+}$, Dy^{3+} samples were obtained by varying the Al/Sr ratios during preparation.

4.2.4 UV-vis analysis

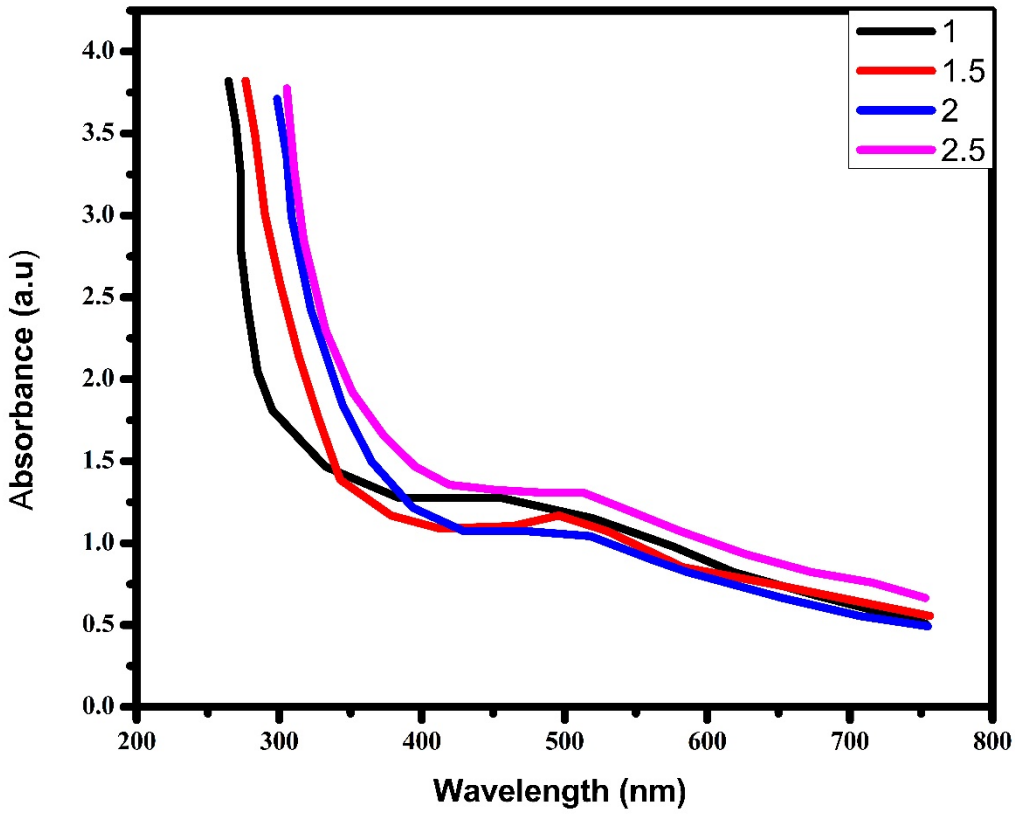

Figure 4.7: UV–Vis absorbance spectra of $SrAl_2O_4:Eu^{2+},Dy^{3+}$ phosphor.

Figure 4.7 illustrates the absorbance of the $SrAl_2O_4:Eu^{2+},Dy^{3+}$ material that was produced and developed using various Al/Sr molar ratios. The NPs' absorbance was determined within the wavelength ranging from 200 to 750 nm. The absorption spectra of all the samples exhibited absorption edges at 400 nm, which aligned with the optical band gap of $SrAl_2O_4:Eu^{2+},Dy^{3+}$. The absorption band edges shifted to greater wavelengths when the Al/Sr molar ratio increased due to the size impact caused by nanostructures. The red shifting is also said to be associated with changes in the size of the crystallites, which can be linked to an enhancement in the degree of purity of the nanoparticles' crystal structure. The red shift of the absorption edges of $SrAl_2O_4:Eu^{2+},Dy^{3+}$ can be ascribed to the inter-band gap formed by europium ions and dysprosium ions, or it may be due to bigger crystallite sizes.

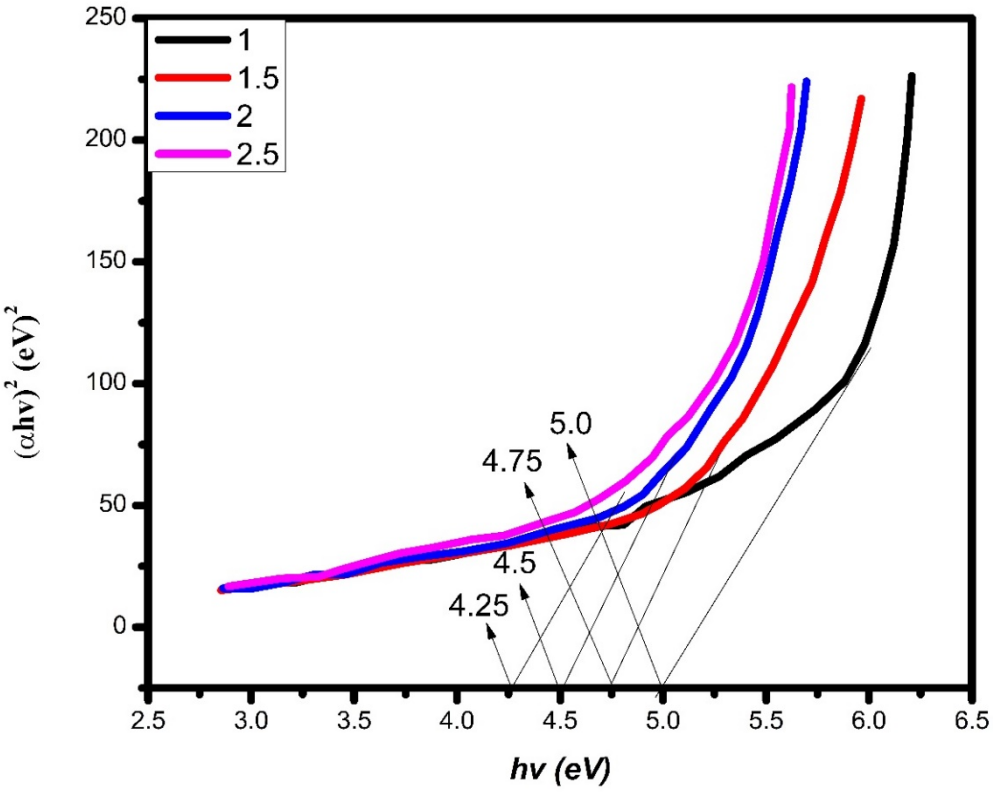

Figure 4.8: Band gap plot of $SrAl_2O_4:Eu^{2+},Dy^{3+}$ NPs Prepared at varying Al ratios

Optical band-gap energy (Eg) of the nanoparticles (NPs) in their original state was calculated using a mathematical derivative of the absorption coefficient (α). An analysis was conducted on the relationship between optical density and wavelength in order to determine the optical energy band gap, utilizing the Tauc correlation [96].

$$\alpha hv = A(hv - Eg)^n \qquad (6)$$

The value A in this context is derived from Fermi's golden rule, that describes electronic shifts between fundamental energy bands. In direct acceptable shifts, the exponent n is equal to 1/2, whereas for permissible indirect transitions, n is equal to 2. The term "Eg" refers to the energy difference between the valence band and the conduction band in optics. The optical band gap values were determined by projecting the linear portion of the Tauc plot to the energy (hv) axis, as shown in Figure 4.8..

The band gap of $SrAl_2O_4:Eu^{2+},Dy^{3+}$ nanoparticles was estimated to be 5.0, 4.75, 4.5, and 4.25 eV for Al/Sr molar ratios of 1, 1.5, 2, and 2.5 mol%, respectively. The decline in the optical band gap obtained when the Al/Sr molar ratio increases can be attributed to changes in lattice defects and stress [12].

4.3 The influence of Dy^{3+} concentrations on the structural and optical properties $Sr_{0.97}Al_2O_4:Eu^{2+}_{0.01},Dy^{3+}_{0.02}$

4.3.1 Experimental Procedure

Dy3+ co-doped SrAl2O4:Eu2+,Dy3+ phosphor was prepared by the solution combustion method. The Sr(NO3)2,Al(NO3)3·9H2O,Eu(NO3)3·6H2O and (Dy(NO3)3·5H2O urea(CH4N2O) and boric acid (H3BO3) were taken as starting materials and were dissolved in 10ml of deionized water and stirred for 30 minutes. The doping concentrations of the Dy3+ ions were 0.1, 0.2, 0.4, 0.6, 0.8 mol%, respectively. After stirring, the transparent solution was taken into a muffle furnace maintained at a temperature of 700℃. The solution boiled and underwent dehydration, followed by decomposition with the escape of large amount of gasses (oxides of carbon, nitrogen and ammonia) and then a white foamy and voluminous ash was produced. The whole process was over within less than 5 min, after the product was cooled to room temperature. The foamy powder was crushed into a powder using a pestle mortar and the obtained white powder was used for characterization. The techniques used for characterization were X-ray diffraction (XRD, D8 advanced AXSGmbH) to identify the crystalline properties of the particles, and Fourier Transform infrared spectroscopy (FTIR Bruker Series) to identify the types of chemical bonds

4.3.2 Structural analysis (XRD)

Figure 4.9 shows diffraction profiles of $SrAl_2O_4:Eu^{2+},Dy^{3+}$ nanophosphors doped with Dy^{3+}. They were a good match alongside the standard JCPDS data file (No. 34-0379) for the $SrAl_2O_4:Eu^{2+},Dy^{3+}$ monoclinic phase with space group P_{21}. And on top of that, there was extra peak at 25.8˚ attributed by incomplete combustion of the precursors. However, there was no peak linked to dopants ions. This suggests that dopant ions were spread out evenly in the host[97]. As the Dy^{3+} concentration was raised, no new peaks corresponding to other phases were seen. This suggests that the structure of the $SrAl_2O_4:Eu^{2+},Dy^{3+}$ nanomaterial is very stable. As the Dy content

went up, the diffraction peaks got less intense, but they didn't move much in terms of where they were. It's possible that the changes in the peak strength were caused by defects appearing as the Dy^{3+} concentration rose. Furthermore, it has been observed that when the Dy^{3+} ratio rises, the peak broadens, as indicated by the full width at half maximum (FWHM). The results demonstrate that as the quantity of the co-dopant rises, the material loses crystallinity as the intesisty of the peaks fall. The well-known Debye-Scherrer equation (2) was used to determine the crystallite size D of the $SrAl_2O_4$ phosphor.

The crystallites sizes were measured to be 32.23, 31.69, 30.99, 30.75, and 29.77 nm as the Dy^{3+} concentration increased. An increase in Dy concentration leads to a broadening of XRD peaks (figure 4.10), suggesting a reduction in the crystallite size of the nanomaterial. Both the lattice strain (ε) and crystallite size D were determined. This strain may have developed as a result of the existence Dy^{3+}dopant. The predicted strain rose as the dopant levels rose, as seen in Table4.4. The discrepancy in crystallite size obtained from the methods is due to the Williamson and Hall accounting for broadened produced by tensile strain factors. All approaches' outcomes showed that a rise in doping from 0.1 % to 0.8 % led to a reduction in crystal size. Various studies have revealed a consistent pattern of crystal size alteration in Dy^{3+} doped $SrAl_2O_4$ nanoparticles. The decrease in $SrAl_2O_4$ crystal size is observed as the $SrAl_2O_4$ doping ratio rises, suggesting that the growth was hindered by introducing Dy^{3+} ions into the Sr site. This occurs because the Dy^{3+} ions are integrated in the host lattice.., which generates additional nucleation sites, leading to increased lattice strain and slowing down crystal formation. Due to microstructural strain and other defects, the dislocation density using equation (5) rises with higher levels of Dy^{3+} doping in the host lattice.

Table 4.4: Lattice constant, crystallite sizes and strain in the $SrAl_2O_4:Eu^{2+},Dy^{3+}$ at varying Dy^{3+} ratio

Doping concentration	Scherrer's method D (nm)	Dislocation density X10^{14} lines/m^2	W-H method D (nm)	Strain	Lattice parameter (nm)	Energy Band energy (eV)
0.1	32.23	9.626	33.19	$6.15x10^{-2}$	0.84470	6.5
0.2	31.69	9.958	32.56	$6.25x10^{-2}$	0.84465	6.3
0.4	30.99	10.413	31.38	$6.40x10^{-2}$	0.84380	6.0
0.6	30.75	10.576	30.72	$6.45x10^{-2}$	0.84360	5.7
0.8	29.77	11.128	29.81	$6.67x10^{-2}$	0.8420	5.5

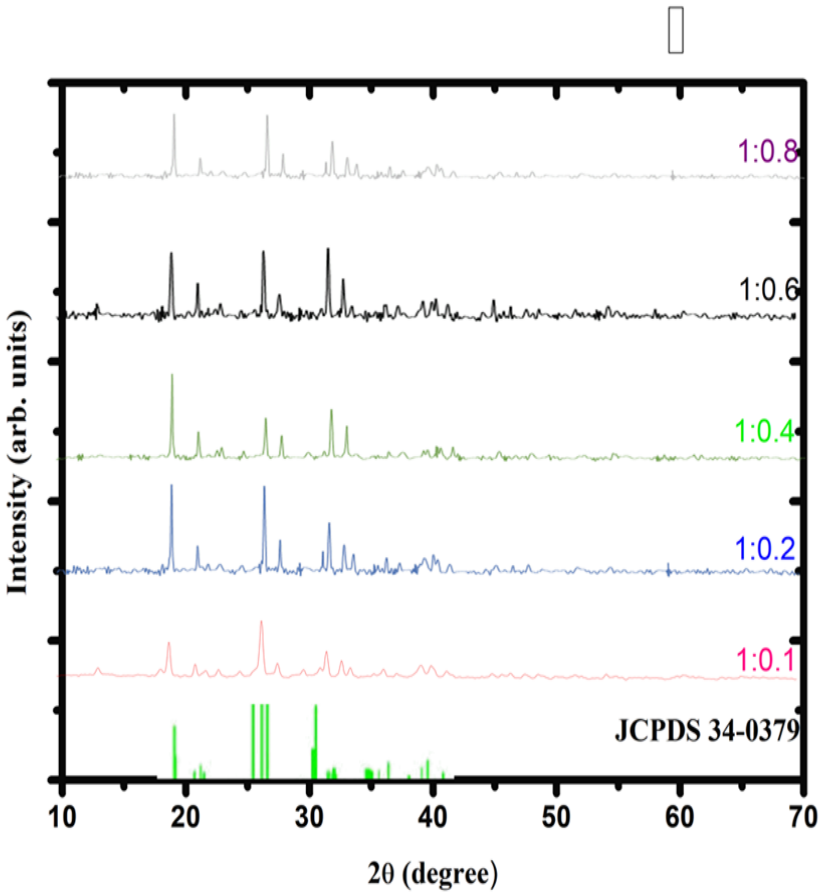

Figure 4.9: XRD of co-doped profiles of $SrAl_2O_4:Eu^{2+}$, Dy^{3+} at varyig concentration of dy 0.1 % to 0.8 %

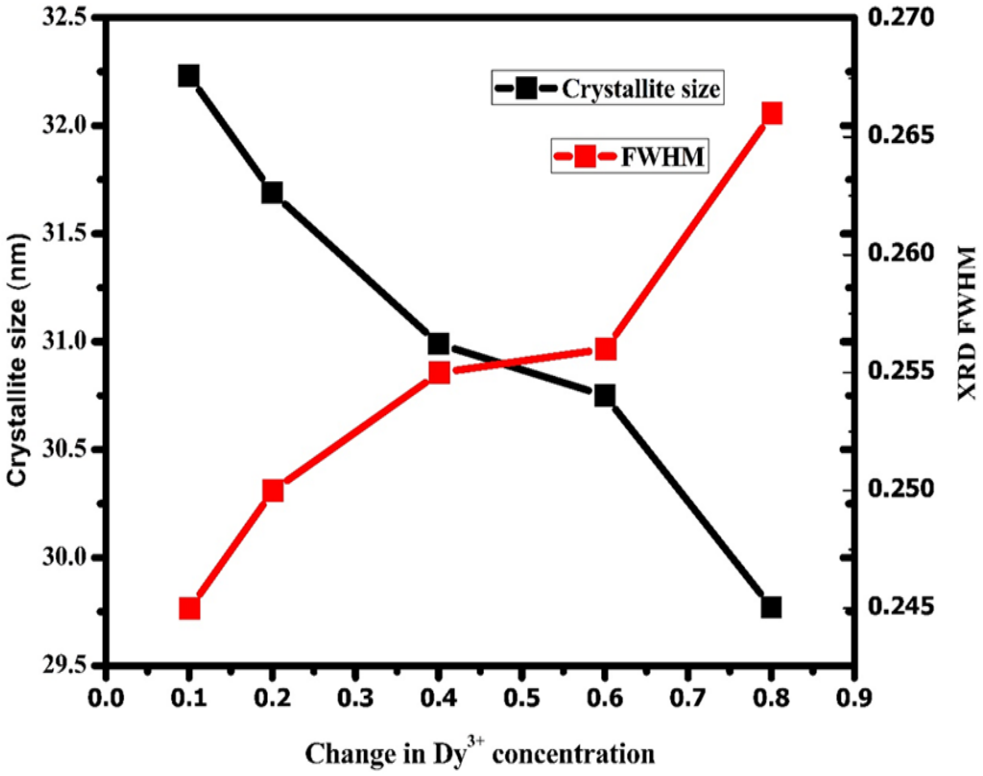

Figure 4.10: Change of crystallite sizes, XRD FWHM with varying concentration of Dy^{3+}

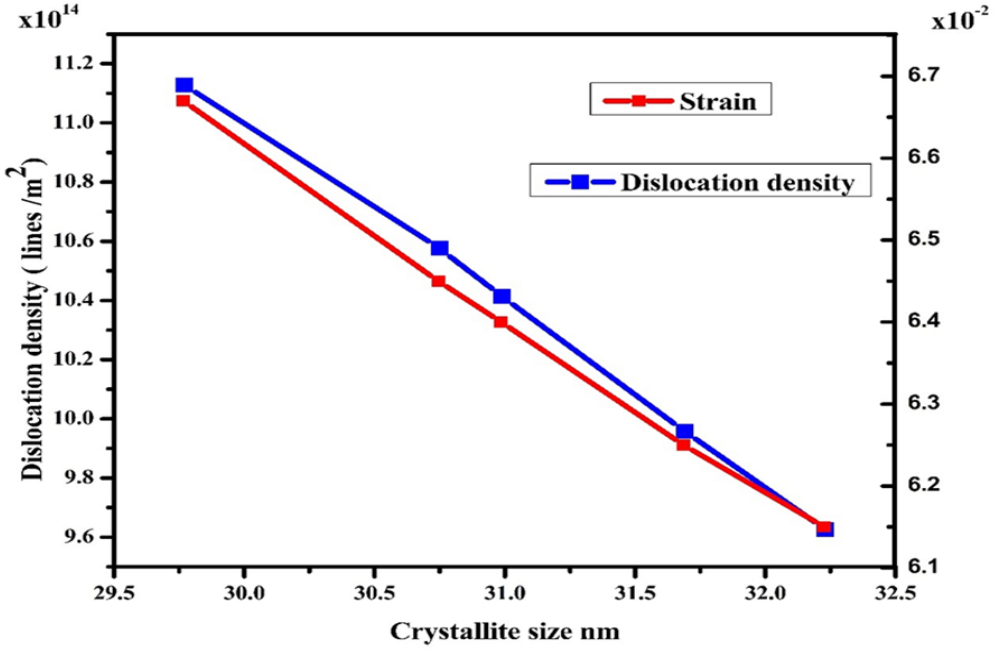

Figure 4.11: Variation of dislocation density and strain with crystallite size as Dy^{3+} concentration changes.

4.3.3 Fourier Transform Infrared Spectroscopy

Figure 4.12 displays IR spectrum of the host containing ($0.1 \leq x \leq 0.8$) of Dy used to analyse the functional compounds and vibrational frequencies in the produced NPs. The vibration seen at 570 cm^{-1} is probably ascribed to the Al-O bond vibrations[23]. Absorption band at 770 cm^{-1} and the strong stretching band at 1049 cm^{-1} are likely caused by the stretching of the Sr − O bonds [23]. The prominent peaks at 2882 and 2964 cm^{-1} are probably due to the C=O bond found in carbon II oxide from the environment[31]. The vibration stretching band observed at 3685 cm−1 is due to physically adsorbed water and O–H groups [91] on a solid surface. FTIR spectrum with varying concentrations of dy, exhibiting identical absorption peaks as seen in Figure 4.12. Research suggests that altering Dy^{3+} content by doping does not influence the vibrational frequency of the nanopowders produced.

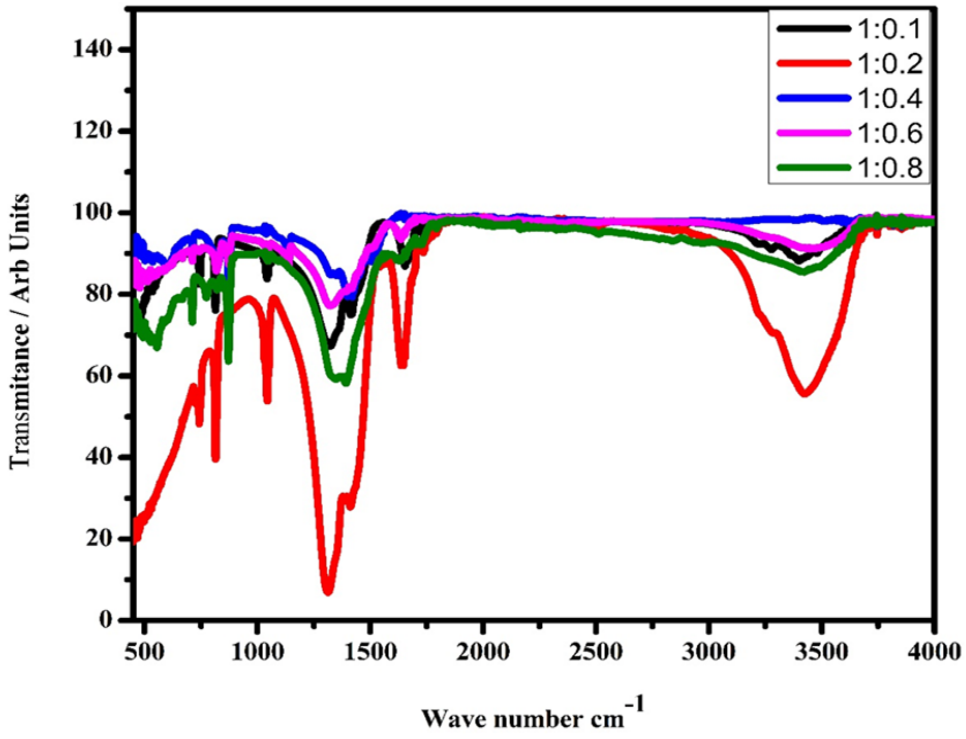

Figure 4.12: FT-IR spectra of $SrAl_2O_4:Eu^{2+}$, Dy^{3+} synthesized at different varying concention of co-dopant

4.3.4 UV-vis analysis

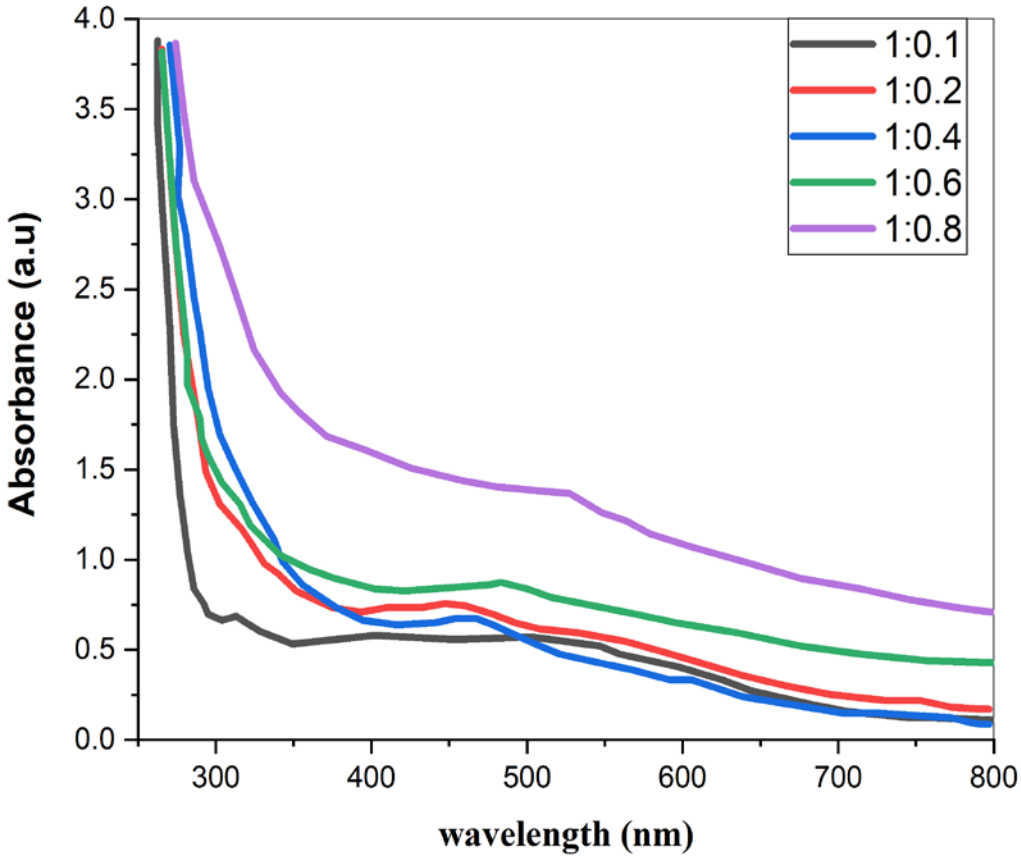

Figure 4.13: Absorption spectra of $SrAl_2O_4:Eu^{2+},Dy^{3+}$ prepared at different Dy^{3+} molar ratios.

UV-vis spectra of $SrAl_2O_4:Eu^{2+},Dy^{3+}$ activated were measured within the 200-800nm wavelength region. The generated Dy^{3+} co-doped samples offer valuable data on the energy bandgap. When molar ratios grew from 0.1 to 0.8, absorption edges and bands shifted toward longer wavelengths. The red shift of absorption peaks shows nanocrystal development[98].It could be attributed as a result of movement of charges across the valence band towards the conduction band of $SrAl_2O_4:Eu^{2+},Dy^{3+}$ nanoparticles [99]. Optical energy bandgap (Eg) of the produced materials was estimated using Tauc's plot shown in figure 4.13.

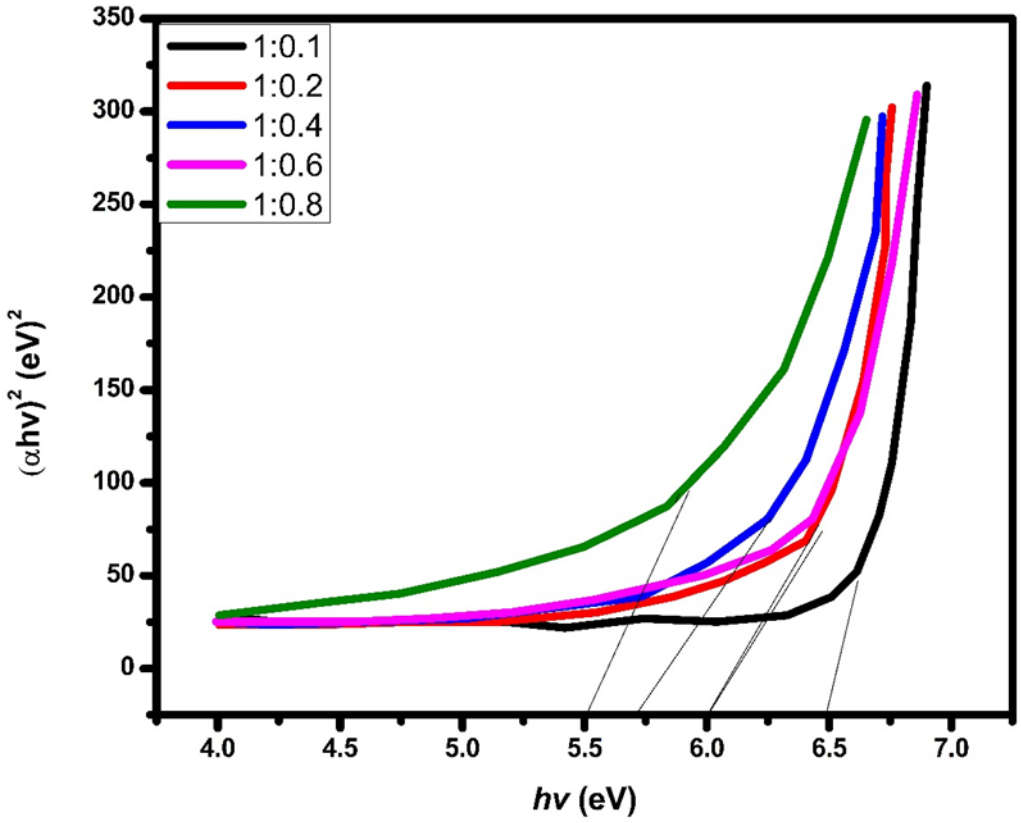

Figure 4.14: Tauc plot ((αhv)^2 vs hv) of varying concentration of Dy to establish the band gap energy of the $SrAl_2O_4:Eu^{2+}$, Dy^{3+} NPs

To determine the bandgap, we prolong the straight-line section of the αhv against the hv graph to zero, with hv. The bandgap magnitude reduced from 6.5 to 5.5 eV when the amount of Dy^{3+} dopant increased from 0.1% to 0.8% (Table 1). Prior studies have also documented a reduction in the bandgap when doping $SrAl_2O_4:Eu^{2+},Dy^{3+}$ [100]. The absorption edge shifts towards longer wavelengths as the concentration of Dy^{3+} ions in the strontium aluminate lattice increases. Doping generates impurities band intensities within strontium aluminate co-dopant contaminants in the $SrAl_2O_4:Eu^{2+},Dy^{3+}$ formation may result in a reduction in bandgap energy, causing the formation of novel interaction centers with lower emitting potential [101]. Higher levels of Dy^{3+} ions cause electron transfer to move across the occupied VB valence band into novel coupling centres instead of the usual shift to the unfilled conduction band [102].

4.4 Optimization of growth parameters.

Optimization of the growth parameters are key in determining the effectiveness of the synthesized phosphor as an information signage on occupational safety and health. The analytical results showed that $700℃$ favoured most promising structural and opitical properties.

When the concentration of Eu^{2+} ion is fixed, the number of electron-hole pairs is fixed. As the concentration of Dy^{3+} ion increases in a range, the number of the Dy^{3+} traps increases, and the traps capture more holes. However, if the doped amount of Dy^{3+} is too large$\geq 0.6\ mol\ \%$ it may result in concentration quenching and 0.4 mol % showed the optimum conditions.

In the light of all these results, phosphor composition in the samples containing different ratios of the host material. The sample with 2 mol % Al/Sr mole ratio designated as the optimum sample that favoured the formation of a monoclinic phase of high crystallinity.

CHAPTER FIVE

CONCLUSIONS AND RECOMMENDATIONS

5.1 Conclusions

$SrAl_2O_4:Eu^{2+},Dy^{3+}$ phosphor powders were successfully synthesized using combustion method. This preparation method was found to be more efficient because the phosphors of high efficiency were obtained at temperatures as low as (500 – 700 °C) in a very short period of time (5 min). Different techniques were used to study the structure, optical properties and the stretching mode frequencies of the phosphor powders. The techniques that were used are X-ray diffraction (XRD), UV-vis and Fourier Transform Infrared Spectroscopy (FT-IR).

Samples synthesized at $500℃$ and $600℃$ showed impurities from unreacted components in the X-ray diffraction profile, whereas those synthesized at temperatures at $700℃$ displayed a polycrystalline structure. $SrAl_2O_4:Eu^{2+},Dy^{3+}$. The X-ray diffraction patterns shows that hexagonal structure when $T = 500 - 600℃$ and monoclinic structure when $T \geq 800℃$.

Optical studies using UV-Vis absorption spectroscopy allow us to emphasize on the tunability of the band-gap of the prepared doped $SrAl_2O_4:Eu^{2+},Dy^{3+}$ nanocrystals. Furthermore, optical investigation based on Photoluminescence spectroscopy evidenced the presence of energy transfer between the rare earth dopant and the $SrAl_2O_4:Eu^{2+},Dy^{3+}$ host matrix which was discussed in detail.

5.2 Recommendations for further study

- Due to time constraints, it was not possible to carry out adequate TEM analysis. For most of the investigations undertaken, TEM analysis would go along way in concretizing many of the conclusions arrived at. This is an imperative tool to further gather valuable information on the crucial parameters like, crystallinity, crystallite size and shape.
- Detailed investigation of PL studies, in order to build on the currently study.
- Detailed study need to be undertaken to determine the cost-effectiveness of nanopowders synthesized.

LIST OF PUBLICATIONS

The following papers have been submitted for publication by the following authors; **Victor kadenge**. Kiprotich Sharon., Ali Wako., Millien Kawira.

1. Structural and Optical properties of $SrAl_2O_4:Eu^{2+},Dy^{3+}$ nanoparticles : Influence of growth Temperature. (submitted to journal of Nanochemistry reseach)
2. Effect of Dy^{3+} concentrations on the structural and optical properties of $SrAl_2O_4:Eu^{2+},Dy^{3+}$ NPs. (accepted and published in the journal of Trends In Sciences) https://doi.org/10.48048/tis.2024.8308

REFERENCES

[1] Y. Lu, L. Chen, Q. Zhang, B.A. Goodman, W. Deng, D. Xiong, S. Xu, Luminescence and microstructural characteristics of Eu2O3-doped SrAl2O4 single crystals, Journal of Luminescence, 253 (2023) 119472.

[2] D. Van der Heggen, J.J. Joos, A. Feng, V. Fritz, T. Delgado, N. Gartmann, B. Walfort, D. Rytz, H. Hagemann, D. Poelman, Persistent luminescence in strontium aluminate: a roadmap to a brighter future, Advanced Functional Materials, 32 (2022) 2208809.

[3] S. Huang, M. Shang, M. Deng, Y. Yan, P. Dang, J. Lin, Tunable concentration/excitation-dependent deep-red and white light emission in single-phase Eu 2+-activated Sc-based oxide phosphors for blue/UV-LEDs, Journal of Materials Chemistry C, 10 (2022) 14971-14981.

[4] H.-W. Tseng, W.-C. Tzou, S. Wei, P.-Y. Lin, C.-F. Yang, Effects of synthesis temperature and Eu2O3 concentration on the crystalline phases and photoluminescence properties of SrAl2O4 phosphors, Journal of Materials Research and Technology, 9 (2020) 14051-14060.

[5] S. Chand, R. Mehra, V. Chopra, Recent developments in phosphate materials for their thermoluminescence dosimeter (TLD) applications, Luminescence, 36 (2021) 1808-1817.

[6] Z. Huang, B. Chen, B. Ren, D. Tu, Z. Wang, C. Wang, Y. Zheng, X. Li, D. Wang, Z. Ren, Smart Mechanoluminescent Phosphors: A Review of Strontium-Aluminate-Based Materials, Properties, and Their Advanced Application Technologies, Advanced Science, 10 (2023) 2204925.

[7] P. Tumram, G. Nair, Metal Oxides: Long Persistent Luminescence, in: Luminescent Metal Oxides, CRC Press, pp. 181-212.

[8] L. Li, W. Wang, J. Tang, Y. Wang, J. Liu, L. Huang, Y. Wang, F. Guo, J. Wang, W. Shen, Classification, synthesis, and application of luminescent silica nanoparticles: a review, Nanoscale research letters, 14 (2019) 1-23.

[9] L. Lu, B. Li, S. Ding, Y. Fan, S. Wang, C. Sun, M. Zhao, C.-X. Zhao, F. Zhang, NIR-II bioluminescence for in vivo high contrast imaging and in situ ATP-mediated metastases tracing, Nature communications, 11 (2020) 4192.

[10] M.S. Abdelrahman, H. Ahmed, T.A. Khattab, Optical and Luminescent Properties of Lanthanide-Doped Strontium Aluminates, Advanced Materials for Solid State Lighting, (2023) 333-354.

[11] D.-W. Zhang, M. Li, C.-F. Chen, Recent advances in circularly polarized electroluminescence based on organic light-emitting diodes, Chemical Society Reviews, 49 (2020) 1331-1343.

[12] X. Duan, L. Yi, S. Huang, Structural and Optical Properties of Size and Morphology Controllable Nanoscale SrAl2O4: Eu2+, Dy3+, Integrated Ferroelectrics, 210 (2020) 74-82.

[13] R. Rojas-Hernandez, M. Rodriguez, F. Rubio-Marcos, A. Serrano, J. Fernandez, Designing nanostructured strontium aluminate particles with high luminescence properties, Journal of Materials Chemistry C, 3 (2015) 1268-1276.

[14] N. Saeed, H. Swart, E. Coetsee, Enhancement of near infrared emission of YOF: Ho3+ co-doped with Yb3+, Materials Science and Engineering: B, 303 (2024) 117279.

[15] Y. Murayama, S. Watanabe, M. Akase, K. Matsui, Effects of composition and reduction conditions on persistent luminescence of SrAl2O4: Eu, Dy prepared via a solid-state reaction, Journal of Luminescence, 251 (2022) 119248.

[16] K.L. Morulane, H.C. Swart, D.E. Motaung, A Review on Topical Advancement and Challenges of Indium Oxide Based Gas Sensors: Future Outlooks, Journal of Environmental Chemical Engineering, (2024) 112144.

[17] H.H.-R. Hagemann, J. Afshani, Synthesis, luminescence and persistent luminescence of europium-doped strontium aluminates, in: Handbook on the Physics and Chemistry of Rare Earths, Elsevier, 2021, pp. 163-225.

[18] R. Lazău, R. Ianoș, C. Păcurariu, D.A. Căpraru, A. Racu, V. Cornea, Combustion Synthesis of SrAl2O4: Eu2+, Dy3+ Phosphorescent Pigments for Glow-in-the-Dark Safety Markings, Nanomaterials, 13 (2023) 687.

[19] P. Kumar, G.K. Inwati, M.C. Mathpal, S. Ghosh, W. Roos, H. Swart, Defects induced enhancement of antifungal activities of Zn doped CuO nanostructures, Applied Surface Science, 560 (2021) 150026.

[20] I.P. Sahu, D. Bisen, N. Brahme, R.K. Tamrakar, R. Shrivastava, Luminescence studies of dysprosium doped strontium aluminate white light emitting phosphor by combustion route, Journal of Materials Science: Materials in Electronics, 26 (2015) 8824-8839.

[21] D.M. Saleem, R. Neema, D.B. Chourasia, G. Wani, M.A. Dar, Structural, Optical and Luminescence Studies of SrAl2O4: Eu3, Dy3 Aluminate System, Dy3 Aluminate System.

[22] R. Singh, A. Bedyal, M. Manhas, H. Swart, V. Kumar, Charge compensated CaSr2 (PO4) 2: Sm3+, Li+/Na+/K+ phosphor: Luminescence and thermometric studies, Journal of Alloys and Compounds, 901 (2022) 163793.

[23] Y. Guo, Z. Jiao, L. Cao, S. Li, The Effect of Trivalent Ions on Luminescent Properties of SrAl2O4: Eu2+, Dy3+ Phosphors, in: Journal of Physics: Conference Series, IOP Publishing, 2023, pp. 012009.

[24] B. Cheng, Z. Zhang, Z. Han, Y. Xiao, S. Lei, SrAl2O4: Eu2+, Dy3+ nanobelts: synthesis by combustion and properties of long-persistent phosphorescence, Journal of Materials Research, 26 (2011) 2311-2315.

[25] D. Golja, F. Dejene, M. Hussen, J. Kim, Combustion Synthesis of Nanocrystalline Ba1. 3Ca0. 7SiO4 Semiconductors Using Urea as an Energy Efficient Fuel. Inorganics 2023, 11, 48, in, 2023.

[26] J. Häusler, F.A. Müller, L. Müller, J. Grabow, C. Cleve, C. Lotz, M. Röschlau, P. Bittorf, R. Fromme, I. Kiebert, Preparation of Phosphorescent Eu2+, Dy3+-Doped Strontium Aluminate Nanoparticles by Laser Vaporization for the Modification of Therapeutic Contact Lenses, Advanced Photonics Research, 3 (2022) 2200013.

[27] P.K. Litoriya, S. Kurmi, A. Verma, Structural, optical, morphological and photoluminescence properties of SrAl2O4: Dy by using urea fuel combustion method, Materials Today: Proceedings, 66 (2022) 2044-2049.

[28] D.S. Ahlawat, R. Kumari, Rachna, I. Yadav, Synthesis and characterization of sol–gel prepared silver nanoparticles, International Journal of Nanoscience, 13 (2014) 1450004.

[29] S. Arora, D.S. Ahlawat, D. Singh, DFT estimation of structural parameters and band gaps of III–V (GaP, AlP, InP, BP) and II–VI (BeX, MgX, CdX: X= O, S, Se, Te) semiconductors, Pramana, 97 (2023) 103.

[30] S.P. Rathee, D.S. Ahlawat, S.M.B. Dhas, K. Mauray, B. Singh, I. Bdikin, Investigations on key aspects of solution growth L-alanine strontium chloride trihydrate single crystal for non-linear optical and photonic applications, Solid State Communications, 319 (2020) 114010.

[31] P. Gao, J. Wang, J. Wu, Q. Xu, L. Yang, Q. Liu, Y. Qi, Z. Li, Preparation of SrAl2O4: Eu2+, Dy3+ Powder by Combustion Method and Application in Anticounterfeiting, Coatings, 13 (2023) 808.

[32] D. Kim, Recent developments in lanthanide-doped alkaline earth aluminate phosphors with enhanced and long-persistent luminescence, Nanomaterials, 11 (2021) 723.

[33] M.B. Al-Handawi, S. Polavaram, A. Kurlevskaya, P. Commins, S. Schramm, C. Carrasco-López, N.M. Lui, K.M. Solntsev, S.P. Laptenok, I. Navizet, Spectrochemistry of firefly bioluminescence, Chemical reviews, 122 (2022) 13207-13234.

[34] W.W. Ward, General aspects of bioluminescence, in: Chemi-and Bioluminescence, CRC Press, 2020, pp. 321-358.

[35] M. Yang, J. Huang, J. Fan, J. Du, K. Pu, X. Peng, Chemiluminescence for bioimaging and therapeutics: recent advances and challenges, Chemical Society Reviews, 49 (2020) 6800-6815.

[36] H. Qi, C. Zhang, Electrogenerated chemiluminescence biosensing, Analytical Chemistry, 92 (2019) 524-534.

[37] L. Tu, Y. Xie, Z. Li, Advances in pure organic mechanoluminescence materials, The Journal of Physical Chemistry Letters, 13 (2022) 5605-5617.

[38] A. Qasem, P. Xiong, Z. Ma, M. Peng, Z. Yang, Recent advances in mechanoluminescence of doped zinc sulfides, Laser & Photonics Reviews, 15 (2021) 2100276.

[39] Q. Zhang, Y. Xiong, Q. Shi, Y. Shi, M. Niu, W. Liu, T. Wu, L. Wang, Z. Zhou, Q. Liu, Effect of Ce3+ on the luminescence properties of SrAl2O4: Eu2+, Dy3+ persistent phosphors for alternating current driven light-emitting diodes, Russian Journal of Inorganic Chemistry, 67 (2022) 1442-1450.

[40] A. Karimata, P.H. Patil, R.R. Fayzullin, E. Khaskin, S. Lapointe, J.R. Khusnutdinova, Triboluminescence of a new family of Cu I–NHC complexes in crystalline solid and in amorphous polymer films, Chemical Science, 11 (2020) 10814-10820.

[41] S.J. Kim, F. Yang, H.S. Jung, G. Hong, S.K. Hahn, Mechanoluminescence and Mechanical Quenching of Afterglow Luminescent Particles for Wearable Photonic Display, Advanced Functional Materials, (2024) 2314861.

[42] E.G. Yukihara, A.J. Bos, P. Bilski, S.W. McKeever, The quest for new thermoluminescence and optically stimulated luminescence materials: Needs, strategies and pitfalls, Radiation Measurements, (2022) 106846.

[43] E.G. Yukihara, A.J. Bos, P. Bilski, S.W. McKeever, The quest for new thermoluminescence and optically stimulated luminescence materials: Needs, strategies and pitfalls, Radiation Measurements, 158 (2022) 106846.

[44] S. Zhang, F. Zhao, S. Liu, Z. Song, Q. Liu, An improved method to evaluate trap depth from thermoluminescence, Journal of Rare Earths, (2024).

[45] H. Kaur, N. Kaur, V. Bhatia, H. Singh, D. Kumar, S.P. Singh, The influence of Dy3+ ions on physical, structural, optical, and thermoluminescence characteristics of Li2O–BaO–B2O3–P2O5 glass system, Materials Research Bulletin, 169 (2024) 112519.

[46] A.S. Altowyan, M. Sonsuz, U. Kaynar, J. Hakami, Z. Portakal-Uçar, M. Ayvacikli, M. Topaksu, N. Can, Synthesis and thermoluminescence behavior of novel Sm3+ doped YCa4O (BO3) 3 under beta irradiation, Ceramics International, (2024).

[47] R. Crapanzano, I. Villa, S. Mostoni, M. D'Arienzo, B. Di Credico, M. Fasoli, R. Lorenzi, R. Scotti, A. Vedda, Photo-and radio-luminescence of porphyrin functionalized ZnO/SiO 2 nanoparticles, Physical Chemistry Chemical Physics, 24 (2022) 21198-21209.

[48] H. Nalumaga, J. Schuyt, G. Williams, D. Clarke, S. Chong, The effect of ionising radiation on the photoluminescence and radioluminescence properties of nanoparticle and bulk NaMgF3: Ce, Sm, Journal of Luminescence, 228 (2020) 117645.

[49] J.S. Klein, C. Sun, G. Pratx, Radioluminescence in biomedicine: physics, applications, and models, Physics in Medicine & Biology, 64 (2019) 04TR01.

[50] W. Chewpraditkul, T. Horiai, A. Beitlerova, R. Kucerkova, V. Babin, A. Yoshikawa, W. Chewpraditkul, M. Nikl, Temperature dependence of photo-and radio-luminescence and scintillation properties of Lu2YAl2. 5Ga2. 5O12: Ce, Mg multicomponent garnet crystals, Optical Materials, 147 (2024) 114738.

[51] B.M. Gareev, A.M. Abdrakhmanov, K.S. Vasilyuk, D.I. Galimov, G.L. Sharipov, Single-Bubble Sonoluminescence of Colloidal Suspensions of Europium (II) Salt Nanoparticles, Applied Spectroscopy, 78 (2024) 125-131.

[52] E. Shafia, A. Aghaei, A. Davarpanah, M. Bodaghi, M. Tahriri, S. Alavi, Synthesis and characterization of SrAl2O4: Eu2+, Dy3+ nanocrystalline phosphorescent pigments, Transactions of the Indian Ceramic Society, 70 (2011) 71-77.

[53] R.E. Rojas-Hernandez, F. Rubio-Marcos, M.Á. Rodriguez, J.F. Fernandez, Long lasting phosphors: SrAl2O4: Eu, Dy as the most studied material, Renewable and Sustainable Energy Reviews, 81 (2018) 2759-2770.

[54] D. Jia, W. Jia, D. Evans, W. Dennis, H. Liu, J. Zhu, W. Yen, Trapping processes in CaS: Eu 2+, Tm 3+, Journal of Applied Physics, 88 (2000) 3402-3407.

[55] Y. Zhuang, Y. Lv, L. Wang, W. Chen, T.-L. Zhou, T. Takeda, N. Hirosaki, R.-J. Xie, Trap depth engineering of SrSi2O2N2: Ln2+, Ln3+ (Ln2+= Yb, Eu; Ln3+= Dy, Ho, Er) persistent luminescence materials for information storage applications, ACS applied materials & interfaces, 10 (2018) 1854-1864.

[56] J. Botterman, J.J. Joos, P.F. Smet, Trapping and detrapping in SrAl 2 O 4: Eu, Dy persistent phosphors: Influence of excitation wavelength and temperature, Physical Review B, 90 (2014) 085147.

[57] I. Ayoub, U. Mushtaq, M. Yagoub, S. Som, H.C. Swart, V. Kumar, Structural and optical characteristics of green-emitting BaGd2ZnO5: Tb3+ phosphor for LED applications, Physica B: Condensed Matter, 669 (2023) 415299.

[58] T. Katsumata, R. Sakai, S. Komuro, T. Morikawa, Thermally Stimulated and Photostimulated Luminescence from Long Duration Phosphorescent SrAl2 O 4: Eu, Dy Crystals, Journal of the Electrochemical Society, 150 (2003) H111.

[59] I. Gupta, S. Singh, S. Bhagwan, D. Singh, Rare earth (RE) doped phosphors and their emerging applications: A review, Ceramics international, 47 (2021) 19282-19303.

[60] M. Zhao, Q. Zhang, Z. Xia, Structural engineering of Eu2+-doped silicates phosphors for LED applications, Accounts of Materials Research, 1 (2020) 137-145.

[61] K. Ashwini, H. Premkumar, B.D. Prasad, G. Darshan, H. Nagabhushana, S. Sharma, S. Prashantha, Green emitting SrAl2O4: Tb3+ nano-powders for forensic, anti-counterfeiting and optoelectronic devices, Inorganic Chemistry Communications, 130 (2021) 108665.

[62] J. Jung, H. Park, H.Y. Jung, S.E. Jung, S.G. Kim, T.H. Kim, Y.J. Lim, B.-C. Ku, M. Kim, S.H. Lee, Recent progress in liquid crystal devices and materials of TFT-LCDs, Journal of Information Display, 25 (2024) 121-142.

[63] S. Singh, V. Tanwar, A.P. Simantilleke, D. Singh, Structural and photoluminescent investigations of SrAl2O4: Eu2+, RE3+ improved nanophosphors for solar cells, Nano-Structures & Nano-Objects, 21 (2020) 100427.

[64] M.-Y. Deng, E.-L. Hsiang, Q. Yang, C.-L. Tsai, B.-S. Chen, C.-E. Wu, M.-H. Lee, S.-T. Wu, C.-L. Lin, Reducing power consumption of active-matrix mini-LED backlit LCDs by driving circuit, IEEE Transactions on Electron Devices, 68 (2021) 2347-2354.

[65] A. Fakharuddin, M.K. Gangishetty, M. Abdi-Jalebi, S.-H. Chin, A.R. bin Mohd Yusoff, D.N. Congreve, W. Tress, F. Deschler, M. Vasilopoulou, H.J. Bolink, Perovskite light-emitting diodes, Nature Electronics, 5 (2022) 203-216.

[66] Q. Wu, Y. Xie, F. She, Q. Zhao, J. Ding, J. Zhou, CsBaB3O6: Eu3+ red-emitting phosphors for white LED and FED: crystal structure, electronic structure and luminescent properties, Journal of Rare Earths, 39 (2021) 1040-1048.

[67] J. Xue, Z. Yu, H.M. Noh, J.H. Jeong, B.C. Choi, S.H. Park, B.R. Lee, P. Du, M. Song, Ce3+/Tb3+-coactived NaMgBO3 phosphors toward versatile applications in white LED, FED, and optical anti-counterfeiting, Journal of the American Ceramic Society, 104 (2021) 5086-5098.

[68] W.-L. Zhao, Y.-F. Wang, S.-P. Wan, H.-Y. Lu, M. Li, C.-F. Chen, Chiral thermally activated delayed fluorescence-active macrocycles displaying efficient circularly polarized electroluminescence, CCS Chemistry, 4 (2022) 3540-3548.

[69] V. Castaing, E. Arroyo, A.I. Becerro, M. Ocaña, G. Lozano, H. Míguez, Persistent luminescent nanoparticles: Challenges and opportunities for a shimmering future, Journal of Applied Physics, 130 (2021).

[70] S. Büyüktiryaki, R. Keçili, C.M. Hussain, Functionalized nanomaterials in dispersive solid phase extraction: advances & prospects, TrAC Trends in Analytical Chemistry, 127 (2020) 115893.

[71] S.K. Sharma, J. James, S.K. Gupta, S. Hussain, UV-A, B, C emitting persistent luminescent materials, Materials, 16 (2022) 236.

[72] K. Huang, N. Le, J.S. Wang, L. Huang, L. Zeng, W.C. Xu, Z. Li, Y. Li, G. Han, Designing next generation of persistent luminescence: recent advances in uniform persistent luminescence nanoparticles, Advanced Materials, 34 (2022) 2107962.

[73] R. Tanaka, K. Uematsu, M. Sato, K. Toda, Afterglow improvement of high concentration Dy3+ co-doped SrAl2O4: Eu2+ phosphor prepared by H3BO3 free synthesis using melt quenching method, Journal of the Ceramic Society of Japan, 129 (2021) 372-376.

[74] Y.-F. Xu, D.-K. Ma, M.-L. Guan, X.-A. Chen, Q.-Q. Pan, S.-M. Huang, Controlled synthesis of single-crystal SrAl2O4: Eu2+, Dy3+ nanosheets with long-lasting phosphorescence, Journal of Alloys and Compounds, 502 (2010) 38-42.

[75] O. Hai, X. He, M. Pei, X. Wu, Q. Ren, Improving Afterglow Properties of Sral2o4: Eu2+, Dy3+ by Changing the Morphology of Silver Nanoparticles, Dy3+ by Changing the Morphology of Silver Nanoparticles.

[76] A. Huang, Y. Wu, Z. Pan, B. Wang, X. Liang, Fabrication, characterization, and optimization of the composite long afterglow material Sr2MgSi2O7: Eu2+, Dy3+@ SrAl2O4: Eu2+, Dy3+, Journal of Sol-Gel Science and Technology, 105 (2023) 500-510.

[77] S.Y. Kaya, E. Karacaoglu, B. Karasu, Particle size influence of starting batches on phosphorescence behaviour of Sr4Al14O25 based bluish green phosphors, Advances in Applied Ceramics, 111 (2012) 393-397.

[78] T. Li, Q. Liu, D. Zhu, P. Chen, Y. Jing, J. Wu, H. Chen, D. Hreniak, M. Nikl, J. Li, Fabrication and characterizations of Eu2+-Dy3+ co-doped SrAl2O4 ceramics with persistent luminescence, Journal of the American Ceramic Society, 106 (2023) 5877-5886.

[79] J. Bierwagen, T. Delgado, G. Jiranek, S. Yoon, N. Gartmann, B. Walfort, M. Pollnau, H. Hagemann, Probing traps in the persistent phosphor SrAl2O4: Eu2+, Dy3+, B3+-A wavelength, temperature and sample dependent thermoluminescence investigation, Journal of Luminescence, 222 (2020) 117113.

[80] N. Takeuchi, K. Kishine, Effect of addition of boron on the long afterglow property of SrAl2O4: Eu2+, Dy3+ phosphor, Materials transactions, 62 (2021) 1039-1045.

[81] T. Delgado, N. Gartmann, B. Walfort, F. LaMattina, M. Pollnau, A. Rosspeintner, J. Afshani, J. Olchowka, H. Hagemann, Fundamental loading-curve characteristics of the persistent phosphor SrAl2O4: Eu2+, Dy3+, B3+: the effect of temperature and excitation density, Advanced Photonics Research, 3 (2022) 2100179.

[82] N. Thejavathi, H. Lokesha, K. Nagabhushana, S.H. Tatumi, S. Krishnaveni, Thermoluminescence characteristics of monoclinic SrAl2O4 phosphor prepared by combustion method, Ceramics International, (2024).

[83] R. Zhong, J. Zhang, X. Zhang, S. Lu, X.-j. Wang, Energy transfer and red phosphorescence in strontium aluminates co-doped with Cr3+, Eu2+ and Dy3+, Journal of luminescence, 119 (2006) 327-331.

[84] N.M. Son, N.N. Trac, Synthesis of SrAl2O4: Eu2+ Dy3+ phosphorescence nanosized powder by combustion method and its optical properties, in: Journal of Physics: Conference Series, IOP Publishing, 2009, pp. 012017.

[85] A.H. Wako, F. Dejene, H. Swart, Combustion synthesis, characterization and luminescence properties of barium aluminate phosphor, Journal of rare earths, 32 (2014) 806-811.

[86] M. Lephoto, O. Ntwaeaborwa, S.S. Pitale, H. Swart, J. Botha, B.M. Mothudi, Synthesis and characterization of BaAl2O4: Eu2+ co-doped with different rare earth ions, Physica B: Condensed Matter, 407 (2012) 1603-1606.

[87] L. Cao, W. Li, B. Devakumar, N. Ma, X. Huang, A.F. Lee, Full-spectrum white light-emitting diodes enabled by an efficient broadband green-emitting CaY2ZrScAl3O12: Ce3+ garnet phosphor, ACS Applied Materials & Interfaces, 14 (2022) 5643-5652.

[88] R. Shrivastava, J. Kaur, V. Dubey, B. Jaykumar, S. Loreti, Photoluminescence and thermoluminescence investigation of europium-and dysprosium-doped dibarium magnesium silicate phosphor, Spectroscopy Letters, 48 (2015) 179-183.

[89] X. Zhou, W. Geng, J. Li, Y. Wang, J. Ding, Y. Wang, An ultraviolet–visible and near-infrared-responded broadband NIR phosphor and its NIR spectroscopy application, Advanced Optical Materials, 8 (2020) 1902003.

[90] S. Kiprotich, F. Dejene, M.O. Onani, Effects of growth time on the material properties of CdTe/CdSe core/shell nanoparticles prepared by a facile wet chemical route, Materials Research Express, 9 (2022) 025008.

[91] S. Fouzar, T. Eftimov, I. Kostova, A. Benmounah, A. Lakhssassi, Effects of temperature on the time responses of strontium aluminates, Optical Materials, 122 (2021) 111619.

[92] Y. Zhu, Q. Yu, L. Zheng, Z. Pang, M. Ge, Luminous properties of recycling luminous materials SrAl2O4: Eu2+, Dy3+ based on luminous polyester fabric, Materials Research Express, 7 (2020) 095309.

[93] Y. Parganiha, J. Kaur, V. Dubey, R. Shrivastava, S. Dhoble, Synthesis and luminescence study of BaZrO3: Eu3+ phosphor, Superlattices and microstructures, 88 (2015) 262-270.

[94] J. Pathak, B. Pandey, P. Singh, R. Kumar, S. Kaushik, I.P. Sahu, T.K. Thakur, A. Kumar, Exploring the paradigm of phyto-nanofabricated metal oxide nanoparticles: recent advancements, applications, and challenges, Molecular Biotechnology, (2023) 1-21.

[95] G. Mamatha, B.R. Krushna, J. Malleshappa, S. Sharma, S. Kumar, C. Krithika, N.R. Nadar, D. Francis, K. Manjunatha, S.Y. Wu, Investigating the influence of mono-, di-, and trivalent co-dopants (Li+, Na+, K+, Ca2+, Bi3+) on the photoluminescent properties and their prospective role in data security applications for SrAl2O4: Tb3+ nanophosphors synthesized via an eco-friendly combustion method, Materials Science and Engineering: B, 299 (2024) 117008.

[96] H. Du, V. Castaing, D. Guo, B. Viana, SrAl2O4: Eu2+, Dy3+ doped-nanoparticles prepared by pulsed laser ablation in liquids, in: Oxide-based Materials and Devices XI, SPIE, 2020, pp. 170-177.

[97] Z. Ni, T. Fan, S. Bai, S. Zhou, Y. Lv, Y. Ni, B. Xu, Effect of the Concentration of SrAl2O4: Eu2+ and Dy3+ (SAO) on Characteristics and Properties of Environment-Friendly Long-Persistent Luminescence Composites from Polylactic Acid and SAO, Scanning, 2021 (2021) 1-9.

[98] S. Kiprotich, B. Dejene, M. Onani, Effects of precursor pH on structural and optical properties of CdTe quantum dots by wet chemical route, Journal of Materials Science: Materials in Electronics, 29 (2018) 16101-16110.

[99] M. Nazarov, D. Spassky, M.G. Brik, B. Tsukerblat, About the nature of luminescent bands in undoped and Eu2+ doped SrAl2O4 phosphors, Optical Materials, 145 (2023) 114377.

[100] B.D. Bem, Thermal, structural and luminescent properties of long after-glow MAlxOy: Eu^{2+}, Dy^{3+}(M: Sr, Ba) phosphors, in, University of the Free State, 2010.

[101] Y. Xia, D. Wu, Q. Zhou, L. Qin, X. Xu, Y. Xi, C. Lou, Preparation and Performance Study of Sral2o4: Eu2+, Dy3+ Long Afterglow Phosphor Materials, Dy3+ Long Afterglow Phosphor Materials.

[102] H. Terraschke, M. Franzreb, C. Wickleder, Magnetism and Afterglow United: Synthesis of Novel Double Core–Shell Eu2+-Doped Bifunctional Nanoparticles, Chemistry–A European Journal, 26 (2020) 6833-6838.